

**Higher-order lattice Boltzmann model for thermohydrodynamics**

Mohammad Atif, Manjusha Namburi, and Santosh Ansumali\*

*Jawaharlal Nehru Centre for Advanced Scientific Research, Jakkur, Bangalore 560064, India*

(Received 31 July 2018; revised manuscript received 5 October 2018; published 29 November 2018)

We present an energy conserving lattice Boltzmann model on a body-centered-cubic arrangement for thermohydrodynamics. It exhibits accurate thermohydrodynamic behavior with a high degree of accuracy and is therefore capable of simulating compressible and thermal hydrodynamics. The theoretical requirements and the methodology to construct this model have been described in detail and can be employed to construct even more accurate models. Simulations of canonical test cases related to compressible flows like shock tube and thermoacoustic convection and thermal flows like viscous heat dissipation and the Rayleigh-Bénard convection are performed to demonstrate the effectiveness of the model.

DOI: [10.1103/PhysRevE.98.053311](https://doi.org/10.1103/PhysRevE.98.053311)**I. INTRODUCTION**

The lattice Boltzmann model (LBM) aims to construct simplified kinetic picture on a lattice designed to capture the physics of macroscopic flow through simple local microscale operations [1–3]. This highly efficient and easily parallelizable method is routinely used as an alternative numerical method for applications as wide ranging as fluid turbulence, gaseous microflow, soft matter, polymer dynamics, relativistic flows, etc. [1–20]. However, lower-order LBMs have been so far a successful methodology only for incompressible isothermal hydrodynamics and gaseous microflow in slip flow regime. An extension of LBM for thermohydrodynamics and compressible flows is relatively less successful so far. While the higher-order extension of the LBM for weakly compressible but isothermal situations shows promising results for turbulence [21] and the thermal models in incompressible regime are well established, a uniform framework for thermohydrodynamics valid for compressible flows is not fully developed yet.

In general, the thermal LBMs fall into three categories: the passive-scalar approach [22,23], the two distribution approach [24], and the multispeed approach [25,26]. In the passive-scalar approach one relies on the fact that the temperature equation is like a passive scalar provided viscous heat dissipation and compression work done by the pressure are negligible. In the initial days of development, the multispeed approach, a generalization of the isothermal LBM, was tried [25]. In this approach, one adds additional velocities to the basic LBM to acquire higher-order isotropy and obtain the correct temperature dynamics. This requires a higher-order model with equilibrium distribution which includes higher-order velocity terms. Even though this is a theoretically feasible approach, previous models suffered severe numerical instability and the working range for temperature variation was narrow [26]. A popular methodology for simulating realistic thermal flows in the LBM are the double population models

where one models hydrodynamic on one set of population and solves the energy dynamics on the other lattice [24]. However, these models have been largely restricted to incompressible flows. As extension for compressible hydrodynamics requires multispeed models (models with nonzero components of discrete velocities having multiple magnitudes) where one of the established models for compressible flows has 41 velocities [27], a double distribution function approach would require at least 56 velocities (41 for compressible dynamics, 15 for energy dynamics, so that the derivative computations are done in an isotropic manner [28]). Indeed, there is a trend for using  $D3Q15$ ,  $D3Q19$ , and  $D3Q27$  models for energy dynamics [29–32]. Furthermore, these models contain complicated gradient operator terms in the evolution equation for the temperature and imposing boundary conditions are nontrivial, and thus the simplicity of the isothermal LBM has been compromised [33].

In recent years, multispeed models have seen revival even for isothermal hydrodynamics. The motivation behind these models is their better accuracy in the velocity space (relevant for microflow) and enhanced numerical stability in turbulent flows due to better Galilean invariance (cubically correct hydrodynamics) [27,34]. Most of these higher-order models start from the fact that the LBM is low Mach number discretization (using Gauss-Hermite quadrature) of the Boltzmann equation with Bhatnagar-Gross-Krook (BGK) approximation for the collision [18,35–39]. Recently, an interesting approach has been formulated in Ref. [40], where it is shown that one can formulate the LBM around local reference velocity and local reference temperature. An additional step is the introduction of an interpolation scheme and an implicit iteration for advection.

It is intriguing that conventional multispeed thermal models are known to be unstable while multispeed isothermal models developed in recent years have shown better stability for turbulent flows [21]. In contrast, recent multispeed entropic models are quite stable for both thermal and turbulent flows [41,42]. In these models, an expansion of local equilibrium distribution around the rest state is performed. For the thermal multispeed models, an additional expansion around

\*ansumali@jncasr.ac.in

reference temperature is also involved. These models explicitly impose sixth and/or eighth-order isotropy of the zero velocity and reference temperature equilibrium [18,27]. The enhanced stability of these entropic thermal models suggests that the instability is related to the way the discrete equilibrium is constructed. Indeed, starting from the formal entropic equilibrium, it was shown in Ref. [43] that one should first construct equilibrium at zero velocity but nonzero variation in temperature followed by expansion in Mach number around this state. One would expect such expansion to be more stable than a direct two variable (Mach and deviation from reference temperature) expansion. Finally, it is conjectured that the working temperature range does not change substantially for entropic models unless eighth-order isotropy is imposed and the narrow temperature range is related to the way the discrete velocity models are constructed.

In this paper, we construct a multispeed thermal LBM with 67 velocities in three dimensions and show that this class of models works for temperature variation as large as 50%. In order to do so, we incorporate a number of ideas in the multispeed thermal models. First, we systematically list the restrictions on the equilibrium of the discrete velocity models required to obtain the Navier-Stokes-Fourier equations as the hydrodynamic limit. These conditions are used to show that while sixth-order isotropy of the reference equilibrium (at zero velocity and reference temperature) is a must, one only required the trace of the higher-order moments to match with their corresponding Maxwell-Boltzmann expressions. Additionally, we employ the recently developed body-centered-cubic (bcc) lattice based LBM framework [17]. In contrast to the simple cubic (sc) lattice, the links of the bcc lattice provide better spatial accuracy as well as more accuracy in the velocity space. Next, the discrete equilibrium is constructed using entropic formulation and the series expression is derived as a two step procedure where one starts at the reference state with zero velocity and zero temperature variation. Then, one derives the equilibrium at reference state with zero velocity but nonzero variation in temperature, and finally the nonzero velocity equilibrium is written as series expansion around the previous reference state. This expansion turns out to be more stable than a direct two variable (Mach number and deviation from reference temperature) expansion. Finally, we show accuracy and versatility of the new model by presenting a number of benchmark simulations.

This paper is organized as follows: In Sec. II, we briefly review the kinetic theory (in both the continuous form and its discrete velocity models) and the restrictions on the equilibrium of the discrete velocity models required to obtain the Navier-Stokes-Fourier equations as the hydrodynamic limit. In Sec. III, the isothermal LBM in its traditional form is reviewed, followed by the derivation of the constraints on any energy conserving discrete equilibrium in Sec. IV and the series expansion of the discrete entropic equilibrium in Sec. V. In Sec. VI, we briefly discuss the idea behind the lattice based on a body-centered-cubic arrangement of grid points. In Sec. VII, we propose an energy conserving model based on 67 discrete velocities (hereafter  $RD3Q67$ ). In Sec. VIII, we formulate the kinetic boundary conditions for the proposed model. In order to benchmark the proposed model for compressible and thermal flows, we simulate a number of setups,

beginning with simple transient hydrodynamics in Sec. IX and steady-state heat conduction in Sec. X. Finally, in Sec. XI we simulate a few nontrivial test cases like Sod shock tube, thermoacoustic convection, and the classical Rayleigh-Bénard convection.

## II. BOLTZMANN BGK MODEL AND DISCRETE KINETIC THEORY

The kinetic theory of gases provides the simplest statistical description of the fluid dynamics at the molecular level [44,45]. In the hydrodynamic limit, the continuum Navier-Stokes-Fourier (NSF) description emerges not only from the detailed kinetic description, but also from its simplified models (BGK, Fokker-Planck, etc.) [46,47]. In this section we briefly review the Boltzmann BGK equation [46], its moment chain, and the hydrodynamic limit associated with it. The description is kept generic so that it is valid for the Boltzmann BGK equation and its discrete velocity analogs.

In this kinetic approach, one considers a collection of  $N$  particles and provides the statistical description of their motion. While the molecular velocity  $\mathbf{c}$  is continuous in the kinetic theory of gases, in the discrete velocity models (DVMs) it is restricted to a set  $\mathbf{c} = \{\mathbf{c}_1, \dots, \mathbf{c}_{N_d}\}$  consisting of  $N_d$  vectors [48,49]. The central quantity in the kinetic theory is the single particle probability distribution function  $f(\mathbf{x}, \mathbf{c}, t)$  with  $f d\mathbf{c}$  being probability of finding a particle moving with velocity in the range  $c$  to  $c + dc$  at time  $t$  and location  $\mathbf{x}$ , whereas the central quantity in any DVM is the discrete population set  $f = \{f_1(\mathbf{x}, t), \dots, f_{N_d}(\mathbf{x}, t)\}$ . It is convenient to define inner product between two functions  $\phi(\mathbf{c})$  and  $\psi(\mathbf{c})$  as  $\langle \phi, \psi \rangle = \int d\mathbf{c} \phi(\mathbf{c}) \psi(\mathbf{c})$  in the continuous case and  $\langle \phi, \psi \rangle = \sum_{i=1}^{N_d} \phi_i \psi_i$  in the discrete case.

In  $D$  dimensions, the hydrodynamic fields such as mass density  $\rho$ , the velocity  $\mathbf{u}$ , and the energy density  $e$  are related to the moments of the distribution function (populations in discrete case)

$$\left\langle f, \left\{ 1, \mathbf{c}, \frac{\mathbf{c}^2}{2} \right\} \right\rangle = \{\rho, \rho \mathbf{u}, e\}, \quad (1)$$

with  $e = (\rho u^2 + Dp)/2$ , where the ideal gas equation of state  $p = \rho \theta$  relates the thermodynamic pressure with the scaled temperature  $\theta = k_B T/m$  where  $k_B$  is the Boltzmann constant and  $m$  is the mass of the particle. In what follows, the fluctuating velocity is defined as  $\boldsymbol{\xi} = \mathbf{c} - \mathbf{u}$  and we restrict our discussion to three dimensions ( $D = 3$ ) unless otherwise stated. A few other relevant quantities in thermal hydrodynamics are the stress tensor  $\sigma_{\alpha\beta} = \langle f, \xi_\alpha \xi_\beta \rangle$  and the heat flux  $q_\alpha = \langle f, \xi_\alpha \xi^2/2 \rangle$ , where the symmetrized traceless part  $\overline{A_{\alpha\beta}}$  for any second-order tensor  $A_{\alpha\beta}$  is  $\overline{A_{\alpha\beta}} = (A_{\alpha\beta} + A_{\beta\alpha} - 2/3 A_{\gamma\gamma} \delta_{\alpha\beta})/2$ . It is often convenient to rewrite the stress tensor as  $\sigma_{\alpha\beta} = \langle f, c_\alpha c_\beta \rangle - \rho u_\alpha u_\beta - p \delta_{\alpha\beta}$  and the heat flux as  $q_\alpha = \langle f, c_\alpha c^2/2 \rangle - u_\alpha (e + p) - u_\beta \sigma_{\alpha\beta}$ . For subsequent uses, we also define third moment  $Q_{\alpha\beta\gamma} = \langle f, \xi_\alpha \xi_\beta \xi_\gamma \rangle$  with its traceless part  $\overline{Q_{\alpha\beta\gamma}}$  as

$$\overline{Q_{\alpha\beta\gamma}} = Q_{\alpha\beta\gamma} - \frac{2}{5} (q_\alpha \delta_{\beta\gamma} + q_\beta \delta_{\alpha\gamma} + q_\gamma \delta_{\alpha\beta}). \quad (2)$$

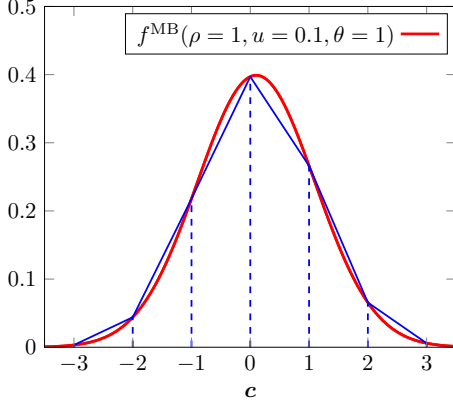


FIG. 1. Finding the discrete equilibrium by evaluating the Maxwell-Boltzmann distribution at discrete points does not conserve the moments. In the figure, the area beneath the curve represents the density, which is different for the Maxwell-Boltzmann distribution and discrete equilibrium as Maxwell-Boltzmann distribution at discrete points.

Similarly, we define the contracted fourth moment  $R_{\alpha\beta} = \langle f, \xi^2 \xi_\alpha \xi_\beta \rangle$ , its traceless part  $\overline{R_{\alpha\beta}} = \overline{\langle f, \xi^2 \xi_\alpha \xi_\beta \rangle}$ , and its trace  $R = \langle f, \xi^4 \rangle$ .

At the equilibrium, the distribution function attains the Maxwell-Boltzmann form [50]

$$f^{\text{MB}} = \rho \left( \frac{1}{2\pi\theta} \right)^{\frac{3}{2}} \exp \left( -\frac{(\mathbf{c} - \mathbf{u})^2}{2\theta} \right). \quad (3)$$

For the Maxwell-Boltzmann distribution, the value of higher-order moments can be evaluated as

$$\begin{aligned} \sigma_{\alpha\beta}^{\text{MB}} &= 0, & q_\alpha^{\text{MB}} &= 0, & Q_{\alpha\beta\gamma}^{\text{MB}} &= 0, \\ \overline{R_{\alpha\beta}^{\text{MB}}} &= 0, & R^{\text{MB}} &= 15\rho\theta^2. \end{aligned} \quad (4)$$

Here, we remind that in the discrete kinetic theory the equilibrium distribution is necessarily different from evaluating the Maxwell-Boltzmann distribution at discrete points (see Fig. 1), and that the moments of the equilibrium distribution show departure from the moments of the Maxwell-Boltzmann distribution [38,39]. Different choice of the discrete velocity set and its equilibrium property leads to different equilibrium moments. The conditions on the equilibrium moments are dictated by the moment chain of the kinetic equation. Subsequent arguments will restrict the choice of the equilibrium moments.

As the aim of the work is to construct an energy conserving thermal model, we intend to highlight the conditions on the equilibrium distribution required to recover the Navier-Stokes-Fourier equations as the hydrodynamic limit of the kinetic equation. Here, we remind that Maxwell's original derivation was based on the arguments of spatial isotropy and independence of the equilibrium distribution from preference to specific direction [50]. Therefore, in order to avoid preference to any specific direction, one imposes a few restrictions on the discrete velocity set  $\mathbf{c}$ . For example, discrete velocity set is chosen such that for each vector  $\mathbf{c}_i \in \mathbf{c}$ , the vector  $-\mathbf{c}_i$  is also present in the set. Similarly, for any vector with components  $(c_{i1}, c_{i2}, c_{i3})$ , all permutations  $\mathcal{P}(c_{i1}, c_{i2}, c_{i3})$  are

also a member of the velocity set [18,51]. These conditions ensure that in the discrete case with any vector  $\phi(\mathbf{c}^2)$  we have

$$\begin{aligned} \langle \phi, c_x^{2n} \rangle &= \langle \phi, c_y^{2n} \rangle = \langle \phi, c_z^{2n} \rangle, \\ \langle \phi, c_x^{2n} c_y^{2m} \rangle &= \langle \phi, c_y^{2n} c_z^{2m} \rangle = \langle \phi, c_z^{2n} c_x^{2m} \rangle, \\ \langle \phi, c_x^{2n+1} \rangle &= \langle \phi, c_y^{2n+1} \rangle = \langle \phi, c_z^{2n+1} \rangle = 0, \end{aligned} \quad (5)$$

where  $n$  and  $m$  are the natural numbers. In this paper, we only consider this class of models.

The time evolution equation for the distribution function in the dilute gas limit is given by the Boltzmann equation [44,50]. However, a simplified and widely used model is the Boltzmann Bhatnagar-Gross-Krook (BGK) equation, which is sufficient to describe Navier-Stokes-Fourier hydrodynamics [46]. The Boltzmann BGK equation representing time evolution of  $f(\mathbf{x}, \mathbf{c}, t)$  is

$$\begin{aligned} \partial_t f(\mathbf{x}, \mathbf{c}, t) + (\mathbf{c} \cdot \nabla) f(\mathbf{x}, \mathbf{c}, t) \\ = -\frac{1}{\tau} [f(\mathbf{x}, \mathbf{c}, t) - f^{\text{eq}}(\rho(\mathbf{x}, t), \mathbf{u}(\mathbf{x}, t), \theta(\mathbf{x}, t))], \end{aligned} \quad (6)$$

with  $\tau$  as the collisional relaxation time and the equilibrium distribution  $f^{\text{eq}}$ . In the continuous case  $f^{\text{eq}}$  is taken as  $f^{\text{MB}}$ , however, in the discrete case  $f^{\text{eq}}$  should be the minimizer of the discrete  $H$  function [39,52,53]. In this section, we distinguish between  $f^{\text{eq}}$  and  $f^{\text{MB}}$  to highlight properties of  $f^{\text{eq}}$  of an arbitrary DVM needed to derive Navier-Stokes-Fourier equations. The conservation laws obtained upon integrating the Boltzmann BGK equation are

$$\begin{aligned} \partial_t \rho + \partial_\alpha (\rho u_\alpha) &= 0, \\ \partial_t (\rho u_\alpha) + \partial_\beta (\rho u_\alpha u_\beta + p \delta_{\alpha\beta} + \sigma_{\alpha\beta}) &= 0, \\ \partial_t e + \partial_\beta [(e + p)u_\beta + \sigma_{\beta\gamma} u_\gamma + q_\beta] &= 0. \end{aligned} \quad (7)$$

These equations contain higher-order moments such as the stress tensor and the heat flux. The evolution of the stress tensor obtained by taking the second moment of Eq. (6) is (see Appendix A 3 for derivation)

$$\begin{aligned} \partial_t \sigma_{\alpha\beta} + u_\gamma \partial_\gamma \sigma_{\alpha\beta} + \partial_\gamma \overline{Q_{\alpha\beta\gamma}} + \sigma_{\alpha\beta} \partial_\gamma u_\gamma + 2\overline{\sigma_{\gamma\beta} \partial_\gamma u_\alpha} \\ + 2p \overline{\partial_\beta u_\alpha} + \frac{4}{5} \overline{\partial_\beta q_\alpha} = \frac{1}{\tau} (\sigma_{\alpha\beta}^{\text{eq}} - \sigma_{\alpha\beta}). \end{aligned} \quad (8)$$

Similarly, the evolution of heat flux obtained by taking the third moment of Eq. (6) is (see Appendix A 4 for derivation)

$$\begin{aligned} \partial_t q_\alpha + \frac{1}{2} \partial_\beta \left( \overline{R_{\alpha\beta}} + \frac{1}{3} R \delta_{\alpha\beta} \right) + \overline{Q_{\alpha\beta\gamma}} \partial_\gamma u_\beta + \partial_\beta (q_\alpha u_\beta) \\ + \frac{7}{5} q_\beta \partial_\beta u_\alpha + \frac{2}{5} q_\alpha \partial_\beta u_\beta + \frac{2}{5} q_\beta \partial_\alpha u_\beta \\ - \frac{5}{2} \frac{p}{\rho} \partial_\alpha p - \frac{\sigma_{\alpha\beta}}{\rho} \partial_\beta p - \frac{5}{2} \frac{p}{\rho} \partial_\theta \sigma_{\alpha\theta} - \frac{\sigma_{\alpha\beta}}{\rho} \partial_\theta \sigma_{\beta\theta} \\ = \frac{1}{\tau} (q_\alpha^{\text{eq}} - q_\alpha). \end{aligned} \quad (9)$$

These evolution equations form the moment chain and can be seen to contain one higher moment than the moment whose evolution they represent, i.e., the evolution of density contains momentum, the evolution of momentum contains the viscous

stress, and so on. In the continuous case this chain goes on to infinity, while in the discrete case the moment chain closes at a finite level and forms a set of  $N_d$  coupled partial differential equations [10,44,49]. In order to obtain the hydrodynamic limit from the equations in the moment chain, following Chapman-Enskog procedure, we expand the time derivative as

$$\partial_t = \partial_t^{(0)} + \tau \partial_t^{(1)} + O(\tau^2), \quad (10)$$

and the nonconserved moments  $M^{\text{fast}}$  about their respective equilibria in order of  $\tau$  as

$$M^{\text{fast}} = M^{\text{eq}}(\rho, \mathbf{u}, \theta) + \tau M^{(1)} + O(\tau^2), \quad (11)$$

where  $M^{\text{fast}} = \{\sigma_{\alpha\beta}, q_\alpha, Q_{\alpha\beta\gamma}, \overline{R_{\alpha\beta}}, R\}$ . Keeping in mind the objective of obtaining the Navier-Stokes-Fourier equations at zeroth and first order of  $\tau$ , a number of comments can be made:

(i) The velocity evolution obtained upon performing algebraic manipulations on Eq. (7) is (see Appendix A 2 for derivation)

$$\partial_t u_\alpha + u_\beta \partial_\beta u_\alpha + \frac{1}{\rho} \partial_\alpha p + \frac{1}{\rho} \partial_\gamma \sigma_{\alpha\gamma} = 0, \quad (12)$$

in which at  $O(\tau^0)$  we obtain

$$\partial_t^{(0)} u_\alpha + u_\beta \partial_\beta u_\alpha + \frac{1}{\rho} \partial_\alpha p + \frac{1}{\rho} \partial_\beta (\sigma_{\alpha\beta}^{\text{eq}} - \sigma_{\alpha\beta}^{\text{MB}}) = 0, \quad (13)$$

from where we see that Euler dynamics up to  $O(u^{n-1})$  is obtained provided  $\sigma_{\alpha\beta}^{\text{eq}} - \sigma_{\alpha\beta}^{\text{MB}} = O(u^n)$ . It is typical to demand that  $\sigma_{\alpha\beta}^{\text{eq}} - \sigma_{\alpha\beta}^{\text{MB}} = O(u^4)$ .

(ii) The temperature evolution can also be obtained upon performing algebraic manipulations on Eqs. (7) (see Appendix A 3 for derivation):

$$\partial_t \theta + u_\alpha \partial_\alpha \theta + \frac{2}{3} \theta \partial_\beta u_\beta + \frac{2}{3\rho} \sigma_{\alpha\beta} \partial_\alpha u_\beta + \frac{2}{3\rho} \partial_\alpha q_\alpha = 0, \quad (14)$$

in which at  $O(\tau^0)$  we obtain

$$\begin{aligned} \partial_t^{(0)} \theta + u_\alpha \partial_\alpha \theta + \frac{2}{3} \theta \partial_\beta u_\beta + \frac{2}{3\rho} (\sigma_{\alpha\beta}^{\text{eq}} - \sigma_{\alpha\beta}^{\text{MB}}) \partial_\alpha u_\beta \\ + \frac{2}{3\rho} \partial_\alpha (q_\alpha^{\text{eq}} - q_\alpha^{\text{MB}}) = 0, \end{aligned} \quad (15)$$

from where we see that the Euler dynamics up to  $O(u^{n-1})$  is obtained provided  $\sigma_{\alpha\beta}^{\text{eq}} - \sigma_{\alpha\beta}^{\text{MB}} = O(u^n)$  and  $q_\alpha^{\text{eq}} - q_\alpha^{\text{MB}} = O(u^n)$ .

(iii) From the evolution of stress given by Eq. (8), after ignoring  $\sigma_{\alpha\beta}^{\text{eq}} - \sigma_{\alpha\beta}^{\text{MB}}$  terms, we have at  $O(1)$

$$\partial_\gamma (\overline{Q_{\alpha\beta\gamma}^{\text{eq}} - Q_{\alpha\beta\gamma}^{\text{MB}}}) + 2p \overline{\partial_\beta u_\alpha} + \frac{4}{5} \overline{\partial_\beta (q_\alpha^{\text{eq}} - q_\alpha^{\text{MB}})} = -\sigma_{\alpha\beta}^{(1)}, \quad (16)$$

which in continuous case yields the Stokes relation  $\sigma_{\alpha\beta}^{(1)} = -2p \overline{\partial_\beta u_\alpha}$ , and from where it can be seen that the accurate form of the viscous stress is recovered up to  $O(u^{n-1})$  if  $q_\alpha^{\text{eq}} - q_\alpha^{\text{MB}} = O(u^n)$  and  $Q_{\alpha\beta\gamma}^{\text{eq}} - Q_{\alpha\beta\gamma}^{\text{MB}} = O(u^n)$ .

(iv) Similarly, after substituting  $R^{\text{MB}} = 15\rho\theta^2$  in the evolution of heat flux given by Eq. (9), we have at  $O(\tau^0)$

$$\begin{aligned} \partial_t^{(0)} (q_\alpha^{\text{eq}} - q_\alpha^{\text{MB}}) + \frac{1}{2} \partial_\beta (\overline{R_{\alpha\beta}^{\text{eq}} - R_{\alpha\beta}^{\text{MB}}}) + \frac{1}{6} \partial_\alpha (R^{\text{eq}} - R^{\text{MB}}) \\ + (\overline{Q_{\alpha\beta\gamma}^{\text{eq}} - Q_{\alpha\beta\gamma}^{\text{MB}}}) \partial_\gamma u_\beta \\ + \partial_\beta [(q_\alpha^{\text{eq}} - q_\alpha^{\text{MB}}) u_\beta] + \frac{7}{5} (q_\beta^{\text{eq}} - q_\beta^{\text{MB}}) \partial_\beta u_\alpha \\ + \frac{2}{5} (q_\alpha^{\text{eq}} - q_\alpha^{\text{MB}}) \partial_\beta u_\beta \\ + \frac{2}{5} (q_\beta^{\text{eq}} - q_\beta^{\text{MB}}) \partial_\alpha u_\beta + \frac{5}{2} p \partial_\alpha \theta = -q_\alpha^{(1)}, \end{aligned} \quad (17)$$

from where it can be seen that the Fourier's law is recovered until  $O(\eta^{n-1})$  if  $R^{\text{eq}} - R^{\text{MB}} = O(\eta^n)$ ,  $Q_{\alpha\beta\gamma}^{\text{eq}} - Q_{\alpha\beta\gamma}^{\text{MB}} = O(\eta^n)$ , and  $q_\alpha^{\text{eq}} - q_\alpha^{\text{MB}} = O(\eta^n)$  where  $\eta = \theta/\theta_0 - 1$ . Also, the above equation at  $u_\alpha = 0$  becomes

$$\frac{1}{6} \partial_\alpha (R^{\text{eq}} - R^{\text{MB}}) + \frac{5}{2} p \partial_\alpha \theta = -q_\alpha^{(1)}, \quad (18)$$

from where it can be seen that the biggest source of error in the Fourier's law is the term  $R^{\text{eq}} - R^{\text{MB}}$ .

Therefore, in order to recover the Navier-Stokes-Fourier equations accurately, we require the equilibrium moments of any DVM to mimic as closely as possible the moments of the Maxwell-Boltzmann distribution. The model proposed later in this work will have

$$\begin{aligned} \sigma_{\alpha\beta}^{\text{eq}} &= -\sigma_{\alpha\beta}^{\text{MB}} + O(u^2 \eta^3), & q_\alpha^{\text{eq}} &= q_\alpha^{\text{MB}} + O(u^3 \eta^3), \\ R^{\text{eq}} &= R^{\text{MB}} + O(\eta^4). \end{aligned}$$

### III. LATTICE BOLTZMANN METHOD FOR ISOTHERMAL FLOWS

The lattice Boltzmann method (LBM), a well-defined hierarchy of approximation to the Boltzmann equation based on discrete velocity sets, is an efficient kinetic scheme to model a range of hydrodynamic applications. Typically, higher-order LBMs perform much better for resolving complex phenomena such as Knudsen boundary layer [43,54,55]. Recent works have indicated that even in the case of turbulence, better performance is obtained due to the fact that the hydrodynamic limit of the higher-order LBM is cubically correct and thus Galilean invariant to the leading order [17,56]. In this section, we review the construction methodology for the LBM.

Similar to other DVM, in LBM the velocity space is discretized into a discrete velocity set  $\mathbf{c}$  with the populations  $f$  as the basic working element. However, unlike other DVMs, LBM builds the kinetic theory in discrete space and time too. In order to do so, the physical space is discretized into a series of grid nodes that together comprise a lattice. At any point on the lattice, the neighboring nodes are located at distance of  $\Delta x = m \mathbf{c}_i \Delta t$ , where  $m$  is a natural number [1,27]. This feature of LBM allows for construction of a numerically attractive algorithm where  $f_i$  successively streams along the grid and collides at the nodes. Furthermore, LBM is typically written for isothermal condition and motivated from the Boltzmann BGK equation, the evolution equation reads as

$$\begin{aligned} f_i(\mathbf{x} + \mathbf{c}_i \Delta t, t + \Delta t) \\ = f_i(\mathbf{x}, t) + \alpha \beta [f_i^{\text{eq}}(\rho, \mathbf{u}) - f_i(\mathbf{x}, t)], \end{aligned} \quad (19)$$

where  $\alpha = 2$  and  $\beta = \Delta t / (2\tau + \Delta t)$  is related to the kinematic viscosity  $\nu$  via relaxation time  $\tau = \nu / \theta_0$ , with  $\theta_0$  as the reference temperature. The above equation can also be derived by trapezoidal integration of discrete velocity model with BGK collision [Eq. (6)] [24]. The entropic formulation of LBM has an extra step where  $\alpha$  is found as the root of the entropy estimate

$$H[f(\mathbf{x}, t) + \alpha(f^{\text{eq}}(\rho, \mathbf{u}) - f(\mathbf{x}, t))] - H[f(\mathbf{x}, t)] = 0, \quad (20)$$

where  $H$  is a convex entropy function. It restores the thermodynamic consistency embedded in the Boltzmann description [43]. This method ensures  $H$  theorem for discrete space-time formulation, and thus leads to a nonlinearly stable solver that is effective in context of flows with sharp gradients. Thus, entropic LBM is quite suitable for the case of thermal and compressible flows where gradients can be sharp [26]. Various numerical techniques have been proposed to ensure the correctness and efficient implementation in this step [34,57–63]. The closed form analytical expression for  $\alpha$  was recently found in Ref. [64].

The choice of the discrete equilibrium distribution  $f_i^{\text{eq}}(\rho, \mathbf{u})$  is considered crucial in LBM. It has to ensure that the macroscopic hydrodynamics equations recovered upon Chapman-Enskog expansion of Eq. (19) agree with the Navier-Stokes equations. The discrete equilibrium is required to conserve the mass and momentum, i.e.,

$$\langle f^{\text{eq}}, \{1, \mathbf{c}\} \rangle = \{\rho, \rho \mathbf{u}\}, \quad (21)$$

and was historically evaluated by projecting the Maxwell-Boltzmann distribution on the Hermite basis to obtain a computationally appealing polynomial expression [11,14,38]

$$f_i^{\text{eq}}(\rho, \mathbf{u}) = w_i \rho \left[ 1 + \frac{u_\alpha c_{i\alpha}}{\theta_0} + \frac{u_\alpha u_\beta}{2\theta_0^2} (c_{i\alpha} c_{i\beta} - \theta_0 \delta_{\alpha\beta}) \right], \quad (22)$$

where the reference temperature  $\theta_0$ , the velocities  $\mathbf{c}_i$ , and the weights  $w_i$  are lattice dependent parameters with

$$w_i > 0, \quad \langle w, 1 \rangle = 1. \quad (23)$$

Substituting Eq. (22) into (21) the parameters  $w_i$ ,  $\mathbf{c}_i$ ,  $\theta_0$  are constrained as

$$\langle w, c_\alpha c_\beta \rangle = \theta_0 \delta_{\alpha\beta} \Rightarrow \langle w, c^2 \rangle = 3\theta_0, \quad (24)$$

where we have used the conditions on moments of weights as specified by Eq. (5). In addition to Eq. (21),  $f_i^{\text{eq}}$  should satisfy a few other constraints in order to recover correct hydrodynamics for low Mach isothermal flows. For example, it is important to ensure that the second moment of  $f_i^{\text{eq}}$  is the same as that obtained from the Maxwell-Boltzmann distribution, i.e.,

$$\langle f^{\text{eq}}, c_\alpha c_\beta \rangle = \rho u_\alpha u_\beta + \rho \theta_0 \delta_{\alpha\beta}, \quad (25)$$

which adds another constraint

$$\langle w, c_\alpha c_\beta c_\gamma c_\kappa \rangle = \theta_0^2 \Delta_{\alpha\beta\gamma\kappa} \Rightarrow \langle w, \{c^2 c_x^2, c^4\} \rangle = \{5\theta_0^2, 15\theta_0^2\}, \quad (26)$$

where  $\Delta_{\alpha\beta\gamma\kappa} = \delta_{\alpha\beta} \delta_{\gamma\kappa} + \delta_{\alpha\gamma} \delta_{\beta\kappa} + \delta_{\alpha\kappa} \delta_{\beta\gamma}$  is the fourth-order isotropic tensor. The well-known models like the  $D3Q15$ ,

TABLE I. Weights corresponding to discrete velocities for the basic models.

Discrete velocity	$D3Q15$	$D3Q19$	$D3Q27$
$(\pm 1, 0, 0), (0, \pm 1, 0), (0, 0, \pm 1)$	1/9	1/18	2/27
$(\pm 1, \pm 1, 0), (\pm 1, 0, \pm 1), (0, \pm 1, \pm 1)$		1/36	1/54
$(\pm 1, \pm 1, \pm 1)$	1/72		1/216

$D3Q19$ , and  $D3Q27$  satisfy these conditions. They have  $\theta_0 = \frac{1}{3}$  and the weights corresponding to their discrete velocities are tabulated in Table I.

As pointed out in Sec. II, it is evident that in the limit of  $\tau \rightarrow 0$ , the zeroth-order hydrodynamic equation is the Euler equation. The Navier-Stokes dynamics is correctly recovered provided

$$\langle f^{\text{eq}}, c_\alpha c_\beta c_\gamma \rangle = \rho u_\alpha u_\beta u_\gamma + \rho \theta_0 (u_\alpha \delta_{\beta\gamma} + u_\beta \delta_{\alpha\gamma} + u_\gamma \delta_{\alpha\beta}). \quad (27)$$

Due to the absence of the cubic term in Eq. (22), the above condition is satisfied only up to linear order by widely used lower-order lattice Boltzmann models [65]. This condition on third moment can be fulfilled if the discrete equilibrium distribution is of the form [27,38,43,66]

$$f_i^{\text{eq}}(\rho, \mathbf{u}) = w_i \rho \left[ 1 + \frac{u_\alpha c_{i\alpha}}{\theta_0} + \frac{u_\alpha u_\beta}{2\theta_0^2} (c_{i\alpha} c_{i\beta} - \theta_0 \delta_{\alpha\beta}) + \frac{u_\alpha u_\beta u_\gamma c_{i\gamma}}{6\theta_0^3} (c_{i\alpha} c_{i\beta} - 3\theta_0 \delta_{\alpha\beta}) \right]. \quad (28)$$

The above expression and Eq. (27) impose further restriction on the weights as

$$\langle w, c_\alpha c_\beta c_\gamma c_\kappa c_\zeta c_\eta \rangle = \theta_0^3 \Delta_{\alpha\beta\gamma\kappa\zeta\eta} \Rightarrow \langle w, \{c_x^2 c_y^2 c_z^2, c_x^4 c_y^2, c_x^6\} \rangle = \{7\theta_0^3, 35\theta_0^3, 105\theta_0^3\}, \quad (29)$$

where  $\Delta_{\alpha\beta\gamma\kappa\zeta\eta}$  is the sixth-order isotropic tensor. However, only very high-order models are known to satisfy such constraint in three dimensions [27].

To summarize, the procedure for constructing models for low Mach isothermal hydrodynamics is to find discrete velocities  $\mathbf{c}_i$  on the lattice whose corresponding equilibrium  $f_i^{\text{eq}}$  mimics the moments of the Maxwell-Boltzmann distribution. The conditions that are considered indispensable for the velocity space discretization, which lead to cubically correct hydrodynamics, are

$$\langle w, \{1, c_\alpha c_\beta\} \rangle = \{1, \theta_0 \delta_{\alpha\beta}\},$$

$$\langle w, \{c_\alpha c_\beta c_\gamma c_\kappa, c_\alpha c_\beta c_\gamma c_\kappa c_\zeta c_\eta\} \rangle = \{\theta_0^2 \Delta_{\alpha\beta\gamma\kappa}, \theta_0^3 \Delta_{\alpha\beta\gamma\kappa\zeta\eta}\}. \quad (30)$$

The popular zero-one-three model proposed in Ref. [67] satisfies  $R^{\text{eq}} = R^{\text{MB}} + O(u^4)$  and was found suitable for isothermal and weakly compressible flows. Another excellent methodology to construct lattices takes the quadrature route and is employed to propose various models in two and three dimensions in Refs. [68,69].

#### IV. ENERGY CONSERVING LBM FOR THERMOHYDRODYNAMICS

The link between series expression used for isothermal equilibrium given by Eq. (28) and the Maxwell-Boltzmann distribution is well understood [38]. The aim of this section is to construct a series expansion of the thermal equilibrium at arbitrary temperature and zero velocity. The discrete distribution from the continuous one is obtained in two steps. First, the local Maxwell-Boltzmann distribution is projected to a finite basis expansion around global Maxwell-Boltzmann distribution around zero velocity and reference temperature  $\theta_0$  to obtain

$$f^{\text{MB}}(\rho, \mathbf{u}, \theta_0, \mathbf{c}) = f^{\text{MB}}(\rho, \mathbf{u} = 0, \theta_0, \mathbf{c}) \times \left( 1 + \frac{\mathbf{c} \cdot \mathbf{u}}{\theta_0} + \frac{(\mathbf{c} \cdot \mathbf{u})^2 - u^2 \theta_0}{2\theta_0^2} + O(u^3) \right). \quad (31)$$

Notice that even the expanded version is consistent with the requirement that conserved moments of the equilibrium distribution are preserved [38]. Then, as the second step, a quadrature evaluation is performed to obtain the discrete equilibrium

$$f_i^{\text{eq}}(\rho, \mathbf{u}, \mathbf{c}) = w_i \frac{f_i^{\text{MB}}(\rho, \mathbf{u}, \theta_0, \mathbf{c})}{f_i^{\text{MB}}(\rho = 1, \mathbf{u} = 0, \theta_0, \mathbf{c})}, \quad (32)$$

where the discrete weights  $w_i$  are the equilibrium at zero velocity and reference temperature.

Following the same idea as the isothermal case, we can evaluate the equilibrium distribution at zero velocity and arbitrary temperature. We first project the local Maxwell-Boltzmann distribution onto a finite basis expansion around the global Maxwell-Boltzmann distribution at reference temperature to obtain

$$\tilde{f}^{\text{MB}}(\rho, \mathbf{u} = 0, \theta, \mathbf{c}) = f^{\text{MB}}(\rho, \mathbf{u} = 0, \theta_0, \mathbf{c}) \frac{1}{(1 + \eta)^{\frac{3}{2}}} \times \exp\left(\frac{\mathbf{c}_i^2 \eta}{2\theta_0(1 + \eta)}\right), \quad (33)$$

where  $\eta = \theta/\theta_0 - 1$ . Now, performing a quadrature evaluation followed by expanding and collecting the terms with like powers of  $\eta$  one obtains

$$\begin{aligned} \tilde{f}_i^{\text{eq}}(\rho, \mathbf{u} = 0, \theta) &= w_i \rho \left( 1 + \frac{\eta}{2\theta_0} (\mathbf{c}_i^2 - 3\theta_0) + \frac{\eta^2}{8\theta_0^2} (\mathbf{c}_i^4 - 10\mathbf{c}_i^2\theta_0 + 15\theta_0^2) \right. \\ &+ \frac{\eta^3}{48\theta_0^3} (\mathbf{c}_i^6 - 21\mathbf{c}_i^4\theta_0 + 105\mathbf{c}_i^2\theta_0^2 - 105\theta_0^3) \\ &+ \frac{\eta^4}{384\theta_0^4} (\mathbf{c}_i^8 - 36\mathbf{c}_i^6\theta_0 + 378\mathbf{c}_i^4\theta_0^2 - 1260\mathbf{c}_i^2\theta_0^3 + 945\theta_0^4) \\ &\left. + O(\eta^5) \right). \end{aligned} \quad (34)$$

The requirement that  $\tilde{f}_i^{\text{eq}}$  conserve mass and energy, i.e.,

$$\langle \tilde{f}^{\text{eq}}, \{1, \mathbf{c}^2\} \rangle = \{\rho, 3\rho\theta\}, \quad (35)$$

is trivially satisfied up to  $O(\eta^4)$  if we impose the following conditions on the weights:

$$\langle w, \{1, \mathbf{c}^2, \mathbf{c}^2\mathbf{c}^2, \mathbf{c}^2\mathbf{c}^2\mathbf{c}^2, \mathbf{c}^2\mathbf{c}^2\mathbf{c}^2\mathbf{c}^2, \mathbf{c}^2\mathbf{c}^2\mathbf{c}^2\mathbf{c}^2\mathbf{c}^2\} \rangle = \{1, 3\theta_0, 15\theta_0^2, 105\theta_0^3, 945\theta_0^4, 10395\theta_0^5\}. \quad (36)$$

The weights, discrete velocities, and  $\theta_0$  of the model proposed later in this work will satisfy the above conditions. The equilibrium at finite velocity can be written as expansion around this zero velocity state. We would like to note that the methodology presented in this work differs from Ref. [67] in not using single expansion in two variables (velocity and deviation from reference temperature).

#### V. DISCRETE ENTROPIC EQUILIBRIUM

In entropic LBM (ELBM), one begins with the convex entropy function of the Boltzmann form  $H = \langle f, \ln(f/w) - 1 \rangle$  and construct equilibrium as its minimizer under the constraints of local conservation laws [Eq. (21)] [16,39,43,52,53,70–72]. This constrained minimization can be performed by getting absolute minimum of the functional

$$\Xi = \sum_{i=1}^{N_d} \left[ f_i \left( \ln \frac{f_i}{w_i} - 1 \right) + \hat{\mu} f_i + \zeta_\kappa c_{i\kappa} f_i + \gamma c_i^2 f_i \right], \quad (37)$$

where  $\hat{\mu}$ ,  $\zeta_\kappa$ ,  $\gamma$  are the Lagrange multipliers associated with mass, momentum, and energy, respectively [39,43]. Solving the minimization problem  $\partial \Xi / \partial f = 0$ , one obtains the equilibrium distribution as

$$f_i^{\text{eq}} = w_i \rho \exp(-\mu - \zeta_\kappa c_{i\kappa} - \gamma c_i^2), \quad (38)$$

where for convenience we have transformed the Lagrange multiplier  $\hat{\mu} = \mu - \ln \rho$ . The five Lagrange multipliers and thus the equilibrium populations  $f_i^{\text{eq}}$  can be found in the explicit form if the system of five equations representing mass, momentum, and energy conservation

$$\sum_{i=1}^{N_d} f_i^{\text{eq}} \left\{ 1, c_{i\alpha}, \frac{c_i^2}{2} \right\} = \{\rho, \rho u_\alpha, e\} \quad (39)$$

were explicitly invertible. However, other than the few special cases such as the *D1Q3* model and its higher dimension extensions *D2Q9* and *D3Q27* [39], the explicit solutions are not known. Therefore, one often uses a numerical route to compute the Lagrange multipliers and thus find the entropic equilibrium [42,73,74].

In this section, we will review the procedure to construct the entropic equilibrium as a perturbation series around a reference state. The series serves two purposes: in any numerical methodology of finding the equilibrium distribution, the series provides a good guess for the Lagrange multipliers (and thus allows faster convergence to the true entropic equilibrium), and the series form can be employed to analyze the hydrodynamic limit. We use this approximate polynomial form of the equilibrium to derive the moments of the equilibrium and comment on its accuracy.

As pointed out earlier, the system given by Eqs. (39) does not render an explicit solution. Therefore, we try

to evaluate the explicit solution at a reference state with mean velocity  $\mathbf{u} = 0$ . We define the Lagrange multipliers at this reference state as  $\mu^{(0)}, \zeta_\kappa^{(0)}, \gamma^{(0)}$ , the equilibrium distribution is  $\tilde{f}_i^{\text{eq}} \equiv f_i^{\text{eq}}(\rho, \mathbf{u} = 0, \theta) = w_i \rho \exp(-\mu^{(0)} - \zeta_\kappa^{(0)} c_{i\kappa} - \gamma^{(0)} c_i^2)$ , and the five conservation equations reduce to

$$\sum_{i=1}^{N_d} \tilde{f}_i^{\text{eq}} \left\{ 1, c_{i\alpha}, \frac{c_i^2}{2} \right\} = \left\{ \rho, 0, \frac{3}{2} \rho \theta \right\} \\ \equiv \left\{ \rho, 0, \frac{3}{2} \rho \theta_0 (1 + \eta) \right\}, \quad (40)$$

where  $\eta = \theta/\theta_0 - 1$ . In the above system of equations, one can group together the terms of discrete velocities  $\mathbf{c}_i$  with the opposite discrete velocities  $-\mathbf{c}_i$  terms in the momentum conservation equations and find the solution  $\zeta^{(0)} = 0$ . Hence,

we obtain

$$\tilde{f}_i^{\text{eq}} \equiv f_i^{\text{eq}}(\rho, \mathbf{u} = 0, \theta) = w_i \rho \exp(-\mu^{(0)} - \gamma^{(0)} c_i^2). \quad (41)$$

However, the other two Lagrange multipliers  $\mu^{(0)}$  and  $\gamma^{(0)}$  can still not be evaluated in the explicit form. Therefore, we choose another reference state with  $\theta = \theta_0$  within this reference state. At the new reference state we define the Lagrange multipliers as  $\mu^{(0,0)}, \gamma^{(0,0)}$ , and it is trivial to check that  $\mu^{(0,0)} = \gamma^{(0,0)} = 0$  satisfies the mass and the energy conservation condition. We first construct the perturbation series for  $\tilde{f}_i^{\text{eq}}$  around this reference state. To this effect, we expand the Lagrange multipliers around  $\mu^{(0,0)}$  and  $\gamma^{(0,0)}$  in powers of  $\eta$ :

$$\mu^{(0)} = \mu^{(0,0)} + \eta \mu^{(0,1)} + \eta^2 \mu^{(0,2)} + \eta^3 \mu^{(0,3)} + \dots, \\ \gamma^{(0)} = \gamma^{(0,0)} + \eta \gamma^{(0,1)} + \eta^2 \gamma^{(0,2)} + \eta^3 \gamma^{(0,3)} + \dots. \quad (42)$$

Substituting Eq. (42) in (41) one obtains

$$\tilde{f}_i^{\text{eq}} = w_i \rho \left( 1 - \eta [\mu^{(0,1)} + \gamma^{(0,1)} c_i^2] - \eta^2 \left[ \mu^{(0,2)} + \gamma^{(0,2)} c_i^2 - \frac{1}{2} (\mu^{(0,1)} + \gamma^{(0,1)} c_i^2)^2 \right] + \dots \right), \quad (43)$$

with the requirement that

$$\left\langle \tilde{f}_i^{\text{eq}}, \left\{ 1, \frac{c_i^2}{2} \right\} \right\rangle = \left\{ \rho, \frac{3}{2} \rho \theta_0 (1 + \eta) \right\}. \quad (44)$$

The Lagrange multipliers evaluated by comparing the terms at every order of  $\eta$  on both sides of Eq. (44) are

$$\mu^{(0)} = \frac{3}{2} \eta - \frac{3}{4} \eta^2 + \frac{3}{6} \eta^3 - \frac{3}{8} \eta^4 + \dots, \quad \gamma^{(0)} = -\frac{1}{2\theta_0} \eta + \frac{1}{2\theta_0} \eta^2 - \frac{1}{2\theta_0} \eta^3 + \frac{1}{2\theta_0} \eta^4 + \dots. \quad (45)$$

The procedure is general enough and can be used to find the series expansion for  $\tilde{f}_i^{\text{eq}}$  up to any arbitrary order in  $\eta$ . The expression accurate up to  $O(\eta^4)$  is

$$\tilde{f}_i^{\text{eq}} = w_i \rho \left[ 1 + \frac{\eta}{2\theta_0} (c_i^2 - 3\theta_0) + \frac{\eta^2}{8\theta_0^2} (c_i^4 - 10c_i^2\theta_0 + 15\theta_0^2) + \frac{\eta^3}{48\theta_0^3} (c_i^6 - 21c_i^4\theta_0 + 105c_i^2\theta_0^2 - 105\theta_0^3) \right. \\ \left. + \frac{\eta^4}{384\theta_0^4} (c_i^8 - 36c_i^6\theta_0 + 378c_i^4\theta_0^2 - 1260c_i^2\theta_0^3 + 945\theta_0^4) \right], \quad (46)$$

provided the lattice parameters satisfy conditions given in Eq. (36). Notice that the above expression is same as Eq. (34) evaluated in Sec. IV.

The next step is to derive the equilibrium distribution at nonzero velocity by expanding the Lagrange multipliers in  $\epsilon$  (representing smallness of the Mach number) as

$$\mu = \mu^{(0)} + \epsilon \mu^{(1)} + \epsilon^2 \mu^{(2)} + \epsilon^3 \mu^{(3)} + O(\epsilon^4), \\ \zeta_\kappa = \zeta_\kappa^{(0)} + \epsilon \zeta_\kappa^{(1)} + \epsilon^2 \zeta_\kappa^{(2)} + \epsilon^3 \zeta_\kappa^{(3)} + O(\epsilon^4), \\ \gamma = \gamma^{(0)} + \epsilon \gamma^{(1)} + \epsilon^2 \gamma^{(2)} + \epsilon^3 \gamma^{(3)} + O(\epsilon^4). \quad (47)$$

Substituting the above expressions in Eq. (38) and collecting terms with various powers of  $\epsilon$ , one obtains

$$f_i^{\text{eq}} = \tilde{f}_i^{\text{eq}} \left( 1 - \epsilon [\mu^{(1)} + \zeta_\kappa^{(1)} c_{i\kappa} + \gamma^{(1)} c_i^2] - \epsilon^2 [\mu^{(2)} + \zeta_\kappa^{(2)} c_{i\kappa} + \gamma^{(2)} c_i^2 - \frac{1}{2} (\mu^{(1)} + \zeta_\kappa^{(1)} c_{i\kappa} + \gamma^{(1)} c_i^2)^2] + \dots \right). \quad (48)$$

The mass, momentum, and energy conservation requirements

$$\langle f^{\text{eq}}, \{1, c_\alpha, c^2\} \rangle = \{\rho, \rho u_\alpha \epsilon, 3\rho\theta + \rho u^2 \epsilon^2\} \quad (49)$$

are compared at various orders of  $\epsilon$  to find the Lagrange multipliers

$$\mu = \mu^{(0)} + \epsilon^2 \mu^{(2)} + O(\epsilon^4), \quad \zeta_\kappa = \zeta_\kappa^{(0)} - \epsilon \frac{u_\alpha}{\theta} + \epsilon^3 \frac{u_\alpha^2}{\theta^2} \mathcal{A} + O(\epsilon^4), \quad \gamma = \gamma^{(0)} + O(\epsilon^4), \quad (50)$$

where  $\mathcal{A} = \langle \tilde{f}_i^{\text{eq}}, c_{ix}^2 c_{iy}^2 \rangle / (3\rho\theta^2) - 1/3$ , provided an additional isotropy condition at the eighth order

$$\langle w, c^4 c_\alpha c_\beta c_\gamma c_\kappa \rangle = 63\theta_0^4 \Delta_{\alpha\beta\gamma\kappa} \quad (51)$$

is imposed. Substituting the Lagrange multipliers in Eq. (48), we obtain the expression for discrete equilibrium accurate up to  $O(\epsilon^3)$ :

$$f_i^{\text{eq}} = \tilde{f}_i^{\text{eq}} \left\{ 1 + \frac{u_\alpha c_{i\alpha}}{\theta} - \frac{u^2}{2\theta} + \frac{1}{2} \left( \frac{u_\alpha c_{i\alpha}}{\theta} \right)^2 + \frac{1}{6} \left( \frac{u_\alpha c_{i\alpha}}{\theta} \right)^3 - \frac{u^2 u_\alpha c_{i\alpha}}{2\theta^2} (1 - \mathcal{A}) \right\}. \quad (52)$$

The moments of the equilibrium distribution can be calculated as

$$\langle f^{\text{eq}}, \{1, c_\alpha, c^2, c_\alpha c_\beta, c^2 c_\alpha\} \rangle = \{\rho, \rho u_\alpha, 3\rho\theta + \rho u^2, \rho\theta\delta_{\alpha\beta} + \rho u_\alpha u_\beta + O(u^2\eta^3), 5\rho\theta u_\alpha + \rho u^2 u_\alpha + O(u^3\eta^3)\}, \quad (53)$$

and they can be seen to match the moments of the Maxwell-Boltzmann distribution up to a high accuracy. Any discrete velocity model whose equilibrium distribution satisfies the above condition will have correct thermohydrodynamic limit. The 41 velocity model of Ref. [27] and the off-lattice 27 velocity model of Ref. [18] have sixth-order isotropy imposed on the moments of their weights.

## VI. CRYSTALLOGRAPHIC LATTICE BOLTZMANN MODEL

Historically, the lattice chosen for the LBM has been the simple cubic (sc) lattice which demands that the grid is refined near the solid body or in zones of extreme flow variations [75,76]. It was recently shown that the optimal discretization of position space for the LBM is a body-centered-cubic (bcc) arrangement of grid points, which led to a new class of models called crystallographic LBM [17]. Figures 2 and 3 depict the building blocks and the links of a bcc lattice in two and three dimensions, respectively. It comprises of two simple cubic (sc) lattices displaced by a distance of  $0.5\Delta x$  in each direction. The two grids are connected via discrete velocities as shown in the figures.

Another well-known fact in the computer graphics literature is that the volume representation (or rendering) is better on the bcc lattice [77]. As the bcc grid has more points at the boundaries, it was also found to represent the boundaries well. To illustrate the difference between sc and bcc lattices, Table II depicts various rendered images on them. Like the traditional sc grids, the bcc grid also preserves the ease of streaming along the links while increasing the local accuracy. A comment about parallelization of bcc grid is order: while parallelizing a bcc grid, we need to communicate outgoing

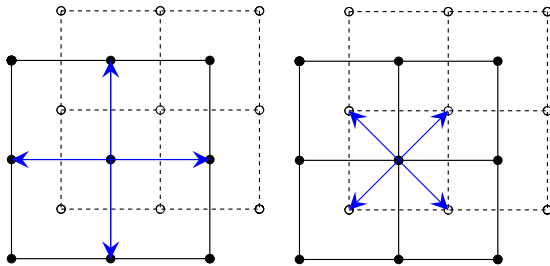


FIG. 2. Building block of a crystallographic lattice in two dimensions, simple cubic links (left) and body-centered links (right) are depicted here.

populations of two layers (in the sc grid outgoing populations from only one layer are communicated). This is illustrated in Fig. 4, where the black lines (solid and dashed) represent the computational grid and the red lines represent the dummy grid. Before implementing the advection routine, the outgoing populations from the computational grid of the Processor A are copied to the dummy grid of Processor B and vice versa. We then implement the advection routine as usual.

The number of grid points for which data need to be communicated (at every face) for parallelization on a bcc grid of size  $2N^3$  is at least  $2N^2$ . On the other hand, for a standard simple cubic grid of size  $(2^{1/3}N)^3$  the number of grid points for which data need to be communicated is  $(2^{1/3}N)^2$ . Thus, there is  $\sim 26\%$  increase in data traffic for bcc method as compared to an sc based method. This cannot lead to any noticeable performance change in communication speed as typical data size for communication in LBM is in the range of  $\sim 20$  MB even for problem size as large as  $256^3$  per node while a modern communication network (InfiniBand) is capable of transferring more than a GB per cycle. Thus, similar to the standard LBM cost of communication is negligible even for bcc based LBM.

Additionally, the artificial closure on the third order moment of single speed models ( $D3Q19$ ,  $D3Q27$ ), i.e.,

$$\langle f, c_\alpha^3 \rangle = c^2 \langle f, c_\alpha \rangle, \quad (54)$$

is avoided due to the crystallographic nature of the lattice. This effect plays an important role in regimes where the Knudsen boundary layer is important [10].

## VII. LBM FOR THERMOHYDRODYNAMICS

In Secs. III and V, it was shown that in order to get the correct thermohydrodynamic limit, the moments of equilibrium distribution have to match the moments of the Maxwell-Boltzmann distribution. The conditions on the moments of the equilibrium translated to constraints on the weights, discrete velocities, and the reference temperature  $\theta_0$  of the lattice [Eqs. (30), (36), and (51)]. To summarize, the constraints are

$$\begin{aligned} \langle w, \{1, c_\alpha c_\beta\} \rangle &= \{1, \theta_0 \delta_{\alpha\beta}\}, \\ \langle w, \{c_\alpha c_\beta c_\gamma c_\kappa, c_\alpha c_\beta c_\gamma c_\kappa c_\zeta c_\eta\} \rangle &= \{\theta_0^2 \Delta_{\alpha\beta\gamma\kappa}, \theta_0^3 \Delta_{\alpha\beta\gamma\kappa\zeta\eta}\}, \\ \langle w, \{c^4 c_\alpha c_\beta c_\gamma c_\kappa, c^{10}\} \rangle &= \{63\theta_0^4 \Delta_{\alpha\beta\gamma\kappa}, 10395\theta_0^5\}, \end{aligned} \quad (55)$$

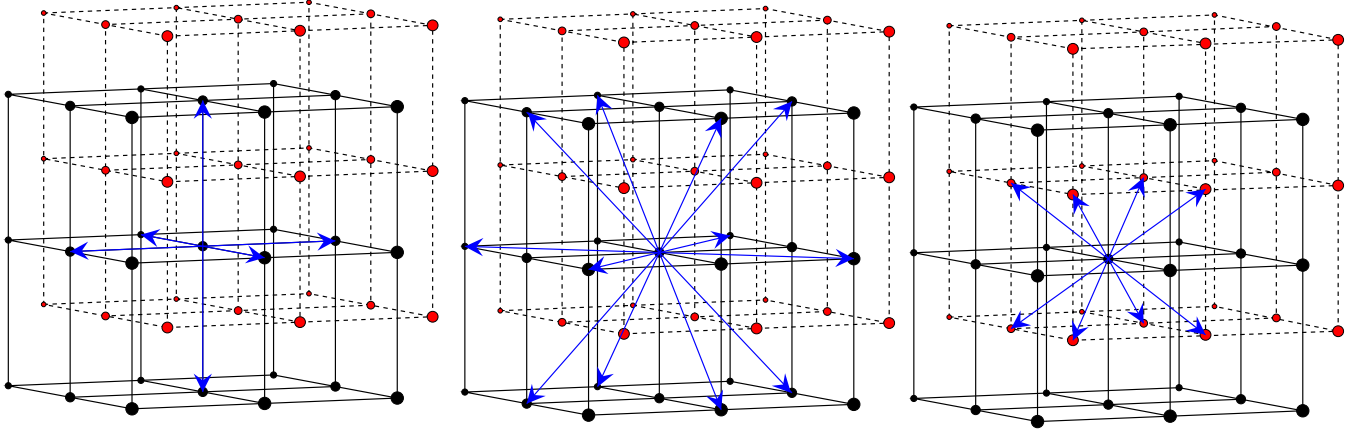


FIG. 3. Building block of a crystallographic grid in three dimensions, simple cubic links (left), face-centered-cubic link (middle), and body-centered links (right). The dashed grid is offset by a distance  $0.5\Delta x$  in each direction.

which are written in the explicit form as a system of 10 equations [using Eq. (5)]

$$\begin{aligned} \langle w, 1 \rangle &= 1, \quad \langle w, c^2 \rangle = 3\theta_0, \quad \langle w, c^4 \rangle = 15\theta_0^2, \\ \langle w, c^2 c_x^2 \rangle &= 5\theta_0^2, \quad \langle w, c^6 \rangle = 105\theta_0^3, \quad \langle w, c^2 c_x^2 c_y^2 \rangle = 7\theta_0^3, \\ \langle w, c^4 c_x^2 \rangle &= 35\theta_0^3, \quad \langle w, c^8 \rangle = 945\theta_0^4, \quad \langle w, c^4 c_x^4 \rangle = 189\theta_0^4, \\ \langle w, c^{10} \rangle &= 10395\theta_0^5. \end{aligned} \quad (56)$$

As the total number of constraints is 10, we will require 8 energy shells that combined with  $w_0$  and  $\theta_0$  will make a total of 10 unknowns. The 8 energy shells chosen are 3 sc, 2 fcc, and 3 bcc. The set of equations has many solutions and we accept the one that satisfies the condition that  $w_i > 0$  and real. The discrete velocities and the weights corresponding to each shell are listed in Table III, and the relevant energy shells are depicted in Fig. 5. The numbers are given to a high accuracy so that the conditions in Eq. (56) can be calculated up to machine precision. The eighth-order moments of the weights that are not imposed in the model are

$$\begin{aligned} \langle w, c_x^8 \rangle &= 104.260789709991 \theta_0^4, \\ \langle w, c_x^6 c_y^2 \rangle &= 13.5316387022748 \theta_0^4, \\ \langle w, c_x^4 c_y^4 \rangle &= 13.5316387022748 \theta_0^4, \\ \langle w, c_x^4 c_y^2 c_z^2 \rangle &= 1.77468903818019 \theta_0^4. \end{aligned}$$

TABLE II. Representation of a sphere, an ellipsoid, and cut section of a red blood cell (RBC) on a sc and bcc lattice at the same resolution. It can be clearly seen that the bcc lattice used by crystallographic LBM represents local curvatures in a more efficient manner as compared to the sc lattice used by the conventional LBM.

Lattice	Sphere	Ellipsoid	RBC
SC			
BCC			

The series approximation of the equilibrium distribution for the set of discrete velocities can be evaluated as

$$\begin{aligned} f_i^{\text{eq}} &= \tilde{f}_i^{\text{eq}} \left( 1 + \frac{u_\alpha c_{i\alpha}}{\theta} - \frac{u^2}{2\theta} + \frac{1}{2} \left( \frac{u_\alpha c_{i\alpha}}{\theta} \right)^2 + \frac{1}{6} \left( \frac{u_\alpha c_{i\alpha}}{\theta} \right)^3 \right. \\ &\quad \left. - \frac{u^2 u_\alpha c_{i\alpha}}{2\theta^2} (1 - \mathcal{A}) \right), \end{aligned} \quad (57)$$

where  $\mathcal{A} = 0.085582531 \eta^3 \theta_0^2 / \theta^2$  and  $\tilde{f}_i^{\text{eq}}$  accurate up to  $O(\eta^4)$  is given by Eq. (34). The equilibrium moments for this model are

$$\langle f_i^{\text{eq}}, c_{i\alpha} c_{i\beta} \rangle = \rho \theta \delta_{\alpha\beta} + \rho u_\alpha u_\beta (1 - \frac{9}{2} \mathcal{A}) + \frac{3}{2} \mathcal{A} \rho u^2 \delta_{\alpha\beta}, \quad (58)$$

$$\langle f_i^{\text{eq}}, c_i^2 c_{i\alpha} \rangle = 5 \rho \theta u_\alpha + \rho u^2 u_\alpha (1 - \frac{3}{2} \mathcal{A} - \mathcal{B}), \quad (59)$$

where  $\mathcal{B} = 0.018853638 \eta^4 \theta_0^3 / \theta^3$ . From the relation  $\sigma_{\alpha\beta}^{\text{eq}} = \langle f_i^{\text{eq}}, c_{i\alpha} c_{i\beta} \rangle - \rho u_\alpha u_\beta - p \delta_{\alpha\beta}$  one obtains

$$\sigma_{\alpha\beta}^{\text{eq}} = \frac{3}{2} \mathcal{A} \rho (u^2 \delta_{\alpha\beta} - 3 u_\alpha u_\beta), \quad (60)$$

and from the relation  $q_\alpha^{\text{eq}} = \langle f_i^{\text{eq}}, c_i^2 c_{i\alpha} / 2 \rangle - u_\alpha (E + p) - u_\beta \sigma_{\alpha\beta}^{\text{eq}}$  one obtains

$$q_\alpha^{\text{eq}} = \rho u^2 u_\alpha (-\frac{3}{2} \mathcal{A} + \frac{1}{2} \mathcal{B}) \quad (61)$$

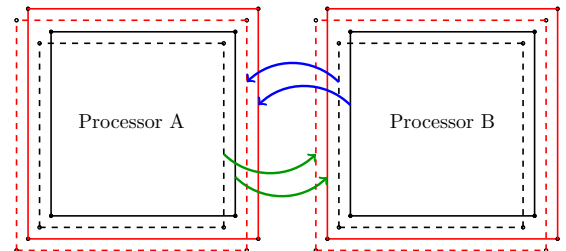


FIG. 4. Communication between two processors on a crystallographic grid.

TABLE III. Energy shells and their corresponding velocities with weights for  $RD3Q67$  model,  $\theta_0 = 0.7487399237215752$ .

Shells	Discrete velocities ( $c_i$ )	Weight ( $w_i$ )
0	(0, 0, 0)	0.062612244873699
sc1	( $\pm 1, 0, 0$ ), ( $0, \pm 1, 0$ ), ( $0, 0, \pm 1$ )	0.07078157740182597
sc2	( $\pm 2, 0, 0$ ), ( $0, \pm 2, 0$ ), ( $0, 0, \pm 2$ )	0.018477181295835005
sc3	( $\pm 3, 0, 0$ ), ( $0, \pm 3, 0$ ), ( $0, 0, \pm 3$ )	0.001159725348044425
fcc2	( $\pm 2, \pm 2, 0$ ), ( $0, \pm 2, \pm 2$ ), ( $\pm 2, \pm 2, 0$ )	0.003016018666364516
fcc3	( $\pm 3, \pm 3, 0$ ), ( $0, \pm 3, \pm 3$ ), ( $\pm 3, \pm 3, 0$ )	0.000023115090889762186
bcc $\frac{1}{2}$	( $\pm 0.5, \pm 0.5, \pm 0.5$ )	0.005042859365786889
bcc1	( $\pm 1, \pm 1, \pm 1$ )	0.03854231746999835
bcc $\frac{3}{2}$	( $\pm 1.5, \pm 1.5, \pm 1.5$ )	0.0012157288848419236

and

$$R^{\text{eq}}(u=0) = \sum \tilde{f}_i^{\text{eq}} c_i^4 = 15\rho\theta^2 + 6.051158073\rho\theta_0^2\eta^4. \quad (62)$$

It can be seen that the error in  $\sigma_{\alpha\beta}^{\text{eq}}$  is of  $O(u^2\eta^3)$ , in  $q_\alpha^{\text{eq}}$  is of  $O(u^3\eta^3)$ , and that in  $R^{\text{eq}}(u=0)$  is of  $O(\eta^4)$ . The viscosity for this model is  $\mu = \tau p$  and the thermal conductivity is  $\kappa = 5/2\mu$ . Further, as pointed out earlier in Eq. (18), the biggest source of error in the Fourier's law is the term containing  $R^{\text{eq}} - R^{\text{MB}}$ , which for the current model is  $6.051158073\rho\eta^4\theta_0^2$ . The error could be reduced by taking into account this deviation via correction of thermal conductivity. The form of corrected thermal conductivity hence is

$$\kappa = \frac{5}{2}\mu \left( 1 + 1.613642153\eta^3 \frac{\theta_0}{\theta} \right). \quad (63)$$

In Sec. XA, we will demonstrate that the corrected form of thermal conductivity indeed increases accuracy at larger temperature deviations. However, in rest of the benchmarking simulations, we do not employ this corrected form.

Finally, we compare the computational cost of the proposed crystallographic  $RD3Q67$  with the standard  $D3Q27$  lattice. In order to have the same resolution as the proposed crystallographic  $RD3Q67$  lattice with  $2N^3$  points, the number of grid points required on a standard  $D3Q27$  lattice is  $(2N)^3 = 8N^3$ . With this understanding, the memory

requirement for the  $RD3Q67$  is approximately  $(2 \times 67)/(8 \times 27) \approx 0.6$  times lower than the standard  $D3Q27$  lattice. To compare the overall performance of the two lattices, we list the time taken for various  $N$  in Table IV. It can be seen that the total time taken for same resolution of the two grids is comparable. However, if we take the same number of points on both the grids, the memory requirement and the time taken by  $D3Q27$  are smaller.

### VIII. KINETIC BOUNDARY CONDITION

In this section, we will present the kinetic diffuse boundary condition [78–81] and its implementation for the proposed model. This boundary condition assumes that upon encountering the wall, the populations completely forget their history. It also assumes that the time spent by the population inside the wall is negligible as compared to any characteristic time. Here, for illustration we will consider the top wall with the normal in the  $y$  direction. The boundary condition for other walls can be formulated in the same manner. For higher-order and crystallographic models, such as the one proposed in the previous sections, populations from multiple layers constitute the outgoing set of populations and need to be properly identified. Note that the incoming and outgoing populations are reflection of each other about the wall.

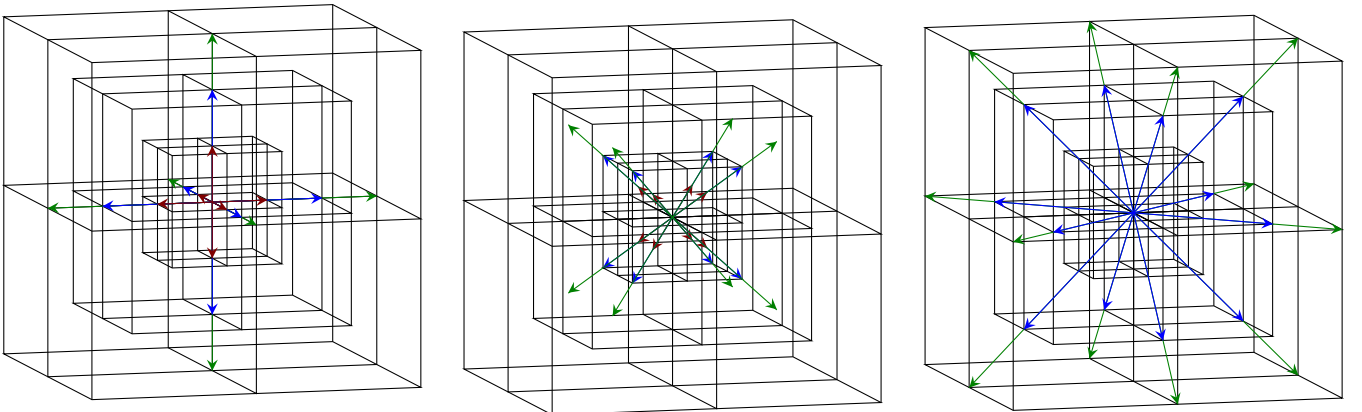


FIG. 5. The energy shells in  $RD3Q67$  model: sc1, sc2, sc3 (left), bcc $\frac{1}{2}$ , bcc1, bcc $\frac{3}{2}$  (center), fcc2, fcc3 (right).

TABLE IV. Time (in seconds) taken for 100 iterations for the proposed  $RD3Q67$  and the standard  $D3Q27$  model on an Intel(R) Xeon(R) CPU E7-4890 v2 @ 2.80GHz processor.

$N$	$RD3Q67 (2N^3)$	$D3Q27 (2N)^3$	$D3Q27 (2N^3)$
64	41.46	36.69	9.44
128	310.84	277.56	70.58
192	1254.95	1219.49	230.60

For the  $RD3Q67$  model, at each wall we encounter six layers  $L_k$ ,  $k = 1 \dots 6$  (see Fig. 6), that have populations missing post streaming and need to be refilled. The total number of incoming and outgoing populations at the layers  $L_1$  to  $L_6$  are 23, 19, 14, 10, 5, 5, respectively. The incoming populations are listed in Table V.

The outgoing populations  $f_{i,L_k}^O$ ,  $k = 1 \dots 6$ , are diffused into the wall and are reflected back in form of a new distribution  $f_{i,L_k}^I$ ,  $k = 1 \dots 6$ . The magnitude of incoming populations  $f_{i,L_k}^I$  is updated via the prescription

$$f_{i,L_h}^I(\mathbf{x}, t) = \frac{\sum_{k=1,3,5} f_{j,L_k}^O(\mathbf{x}, t) |c_{jy}|}{\sum_{k=1,3,5} f_{j,L_k}^{eq}(\rho_w, \mathbf{u}_w, \theta_w) |c_{jy}|} \times f_{i,L_h}^{eq}(\rho_w, \mathbf{u}_w, \theta_w), \quad h = 1, 3, 5$$

$$f_{i,L_h}^I(\mathbf{x}, t) = \frac{\sum_{k=2,4,6} f_{j,L_k}^O(\mathbf{x}, t) |c_{jy}|}{\sum_{k=2,4,6} f_{j,L_k}^{eq}(\rho_w, \mathbf{u}_w, \theta_w) |c_{jy}|} \times f_{i,L_h}^{eq}(\rho_w, \mathbf{u}_w, \theta_w), \quad h = 2, 4, 6 \quad (64)$$

where  $i$  are the populations at each  $L_k$  corresponding to Table V,  $\rho_w = 1$ , and the  $u_w$ ,  $\theta_w$  are wall velocity and temperature, respectively. The above prescription conserves the mass flux at the boundary. The minor fluctuations introduced in mass due to difference  $\sum (f_{i,L_k}^O - f_{i,L_k}^I)$  are eliminated by manipulating the stationary population  $f_0$  at each node. However, the implementation of the complex boundary conditions (anything other than bounce back) is a nontrivial open question. Extensions of the bounce-back boundary condition for imposing temperature and velocity are the diffuse bounce-back boundary condition [82] or the boundary condition proposed in Ref. [83]. We leave the extension of kinetic diffuse boundary condition as the subject of subsequent studies with

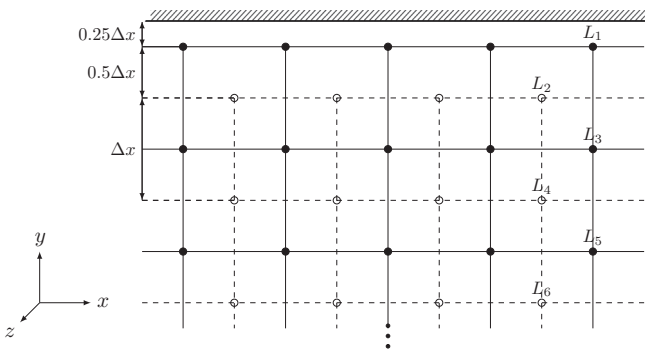


FIG. 6. Populations at each layer that see the top wall and need to be repopulated post streaming are listed in Table V.

TABLE V. Incoming populations at each layer near the top wall.

Layer	Incoming populations $f_{i,L_k}^I$	Total number
$L_1$	$(0, -1, 0), (\pm 1, -1, \pm 1)$ $(0, -2, 0), (\pm 2, -2, 0), (0, -2, \pm 2)$ $(0, -3, 0), (\pm 3, -3, 0), (0, -3, \pm 3)$ $(\pm 1.5, -1.5, \pm 1.5), (\pm 0.5, -0.5, \pm 0.5)$	23
$L_2$	$(0, -1, 0), (\pm 1, -1, \pm 1)$ $(0, -2, 0), (\pm 2, -2, 0), (0, -2, \pm 2)$ $(0, -3, 0), (\pm 3, -3, 0), (0, -3, \pm 3)$ $(\pm 1.5, -1.5, \pm 1.5)$	19
$L_3$	$(0, -2, 0), (\pm 2, -2, 0), (0, -2, \pm 2)$ $(0, -3, 0), (\pm 3, -3, 0), (0, -3, \pm 3)$ $(\pm 1.5, -1.5, \pm 1.5)$	14
$L_4$	$(0, -2, 0), (\pm 2, -2, 0), (0, -2, \pm 2)$ $(0, -3, 0), (\pm 3, -3, 0), (0, -3, \pm 3)$	10
$L_5$	$(0, -3, 0), (\pm 3, -3, 0), (0, -3, \pm 3)$	5
$L_6$	$(0, -3, 0), (\pm 3, -3, 0), (0, -3, \pm 3)$	5

the following suggestion as a possible remedy:

$$f_{i,L_h}^I(\mathbf{x}, t) = \sum_j \frac{f_{j,L_h}^O(\mathbf{x}, t) |\mathbf{c}_j \cdot \mathbf{n}|}{\sum_j f_{j,L_h}^{eq}(\rho_w, \mathbf{u}_w, \theta_w) |\mathbf{c}_j \cdot \mathbf{n}|} \times f_{i,L_h}^{eq}(\rho_w, \mathbf{u}_w, \theta_w), \quad h = 1 \dots 6. \quad (65)$$

In the above equation, each outgoing population will contribute individually to each incoming population, i.e., each incoming population will receive fractions of each of outgoing populations.

In the following sections, we will benchmark the  $RD3Q67$  model and the implementation of the boundary condition for various thermal and compressible flows.

## IX. HYDRODYNAMICS: STARTUP OF SIMPLE SHEAR FLOW

In this section, we consider the startup flow of fluid situated between two parallel plates due to sudden movement of the plate at  $y = 0$  with a constant velocity  $U_{\text{wall}}$  in the  $x$  direction. The other plate at  $y = H$  is kept stationary. The solution for velocity profile at sufficiently long time  $u(y, t = \infty) = U_{\text{wall}}(1 - y/H)$  is linear. The analytical expression for velocity profile is [84]

$$\bar{u}(\bar{y}, \bar{t}) = (1 - \bar{y}) - \sum_{n=1}^{\infty} \frac{2}{n\pi} \exp(-n^2\pi^2\bar{t}) \sin n\pi\bar{y}, \quad (66)$$

where the nondimensionalized variables  $\bar{u} = u/U_{\text{wall}}$ ,  $\bar{y} = y/H$ , and  $\bar{t} = t\nu/H^2$  with  $\nu$  as the kinematic viscosity. This solution is a good test to assess the accuracy of transient dynamics.

This setup was simulated on a grid of size  $8 \times 128 \times 8$  points with wall imposed in the  $y$  directions and periodic boundary conditions in the other two directions. The velocity of the moving wall was taken to be  $U_{\text{wall}} = 0.02$ . The kinematic viscosity was chosen such that the Reynolds number  $\text{Re} = U_{\text{wall}}H/\nu = 512$ . The mean planar velocity at various times is compared against the analytical solution given by Eq. (66) in Fig. 7 and is found to be in good agreement.

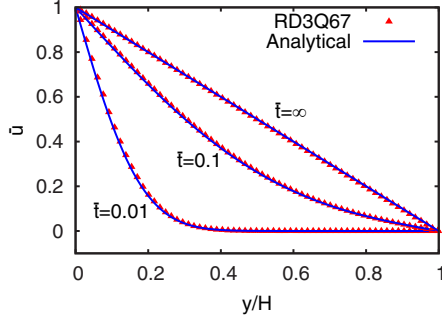


FIG. 7. Nondimensionalized mean planar velocity profiles obtained from *RD3Q67* at various diffusion times compared against the analytical solution.

## X. HEAT CONDUCTION: STEADY STATE

In this section, we consider the steady state for the heat transfer in one and two dimensions. The first two subsections have no flow at the steady state, while the third subsection has nonzero velocity at the steady state.

### A. One-dimensional heat conduction

We consider the steady state for the heat transfer in fluid confined in a one-dimensional domain of height  $H$ . The top wall at  $y = H$  is subjected to a constant elevated temperature  $\theta_{\text{top}}$  and the bottom wall at  $y = 0$  is kept at  $\theta_0$ . The steady-state temperature profile is  $\theta = \theta_0 + (\theta_{\text{top}} - \theta_0)y/H$ . The simulations were performed on a grid of size  $8 \times 32 \times 8$  and Knudsen number  $\text{Kn} = 10^{-3}$ . The relaxation time  $\tau$  is related to  $\text{Kn}$  via  $\text{Kn} = \tau c_s/H$ , where the sound speed  $c_s = \sqrt{(5/3)\theta}$ . The temperature profiles for various values of the temperature jump are given in Fig. 8. It can be seen that the model is accurate and stable for temperatures elevations as high as 50% of  $\theta_0$ . Further, from Fig. 9(left) it can be seen that the magnitude of the  $L^2$  norm decreases upon increasing the grid resolution.

As pointed in Eq. (63), the corrected thermal conductivity is expected to reduce the error. Figure 9(right) contrasts the  $L^2$  norm obtained with using the thermal conductivity correction to without. It can be seen that for lower values of  $\theta_{\text{top}}$  the  $L^2$  norm remains almost the same while for higher values it decreases upon using the thermal conductivity correction.

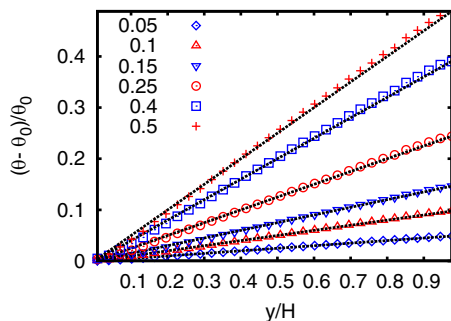


FIG. 8. Temperature plots without including the thermal conductivity correction for different magnitudes of the top wall temperature.

### B. Two-dimensional cavity heated at the top

We consider another simple heat transfer problem in a two-dimensional box of length  $L$  and width  $W$  subjected to an elevated temperatures at the top wall as represented in Fig. 10. The simulations were performed on a grid of size  $256 \times 128 \times 8$  with  $\Delta\theta = 0.10\theta_0$  at  $\text{Kn} = 10^{-3}$ . The rapid heating at the top wall will initiate thermoacoustic convection in the early stages of the simulation, which will be discussed in later sections. We study the system at steady state where the only mode of heat transfer is pure conduction.

The analytical expression for the normalized temperature

$$\bar{\theta}(x, y, t = \infty) = \frac{2}{\pi} \sum_{k=1}^{\infty} \frac{1 - \cos(k\pi)}{k} \sin(k\pi x) \times \frac{\sinh(k\pi y)}{\sinh(k\pi W/L)} \quad (67)$$

is found as the solution of conduction equation. The mean planar temperature profiles at  $x = 0.1, 0.25, 0.5$  and  $y = 0.25, 0.5, 0.75$  are represented in Figs. 11(left) and 11(right), respectively, and are found to match well with the analytical solution.

### C. Viscous heat dissipation

In this section, we consider the steady state of flow induced by wall at  $y = H$  moving with a constant horizontal velocity  $U_{\text{wall}}$  and maintained at a constant elevated temperature  $\theta_{\text{hot}}$ . The lower wall at  $y = 0$  is kept stationary at a constant temperature  $\theta_{\text{cold}} (< \theta_{\text{hot}})$ . This setup is well suited to validate the effect of viscous heat dissipation. Each layer of fluid drags the layer below it due to friction which results in the mechanical energy being converted to thermal heating and, therefore, the heat produced affects the temperature profile in the bulk. The analytical solution for the temperature profile for this setup is [85]

$$\frac{\theta - \theta_{\text{cold}}}{\theta_{\text{hot}} - \theta_{\text{cold}}} = \frac{y}{H} + \frac{\text{Ec}}{2} \frac{y}{H} \left(1 - \frac{y}{H}\right), \quad (68)$$

where the  $\text{Ec} = U_{\text{wall}}^2/(c_p \Delta\theta)$  is the Eckert number that represents the ratio of viscous dissipation to heat conduction with  $c_p = \frac{5}{2}$  as the specific heat at constant pressure and  $\Delta\theta = \theta_{\text{hot}} - \theta_{\text{cold}}$  is the temperature difference between the two walls.

Simulations were performed for  $\text{Ec} = 0.5, 2.0, 5.0$  on a grid size of  $24 \times 128 \times 24$  with  $U_{\text{wall}} = 0.02$  and  $\Delta\theta$  calculated according to respective Eckert numbers. The walls were maintained at temperatures  $\theta_0 + 0.5\Delta\theta$  and  $\theta_0 - 0.5\Delta\theta$  with periodic boundary condition in the other two directions. The normalized mean planar temperature profile at steady state is compared against the analytical solution given by Eq. (68) in Fig. 12 and is found to be in agreement. This suggests that the thermal transport phenomenon is modeled correctly.

## XI. COMPRESSIBLE THERMOHYDRODYNAMICS

A variety of problems of practical interest have velocity and temperature dynamics coupled together. This coupling makes it nontrivial for any fluid solver to represent the physics accurately. The aim section of this section is to benchmark the

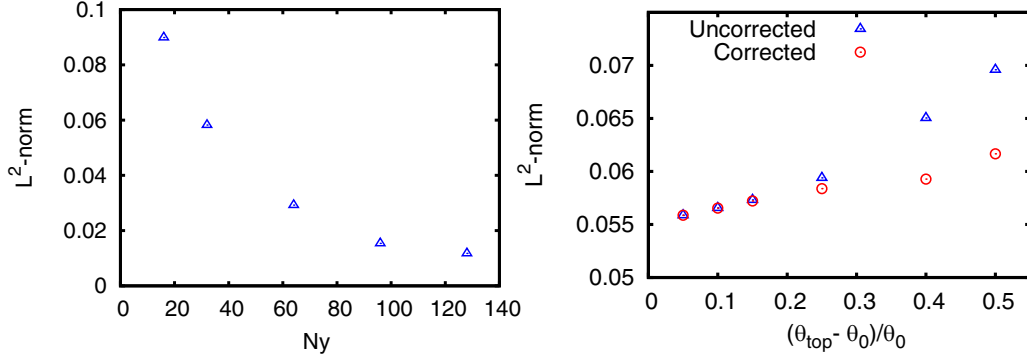


FIG. 9.  $L^2$  norms of temperature: deviation from linear temperature profile at  $\theta_{top} = 1.2\theta_0$  and different grid resolutions (left) and comparison for corrected and uncorrected thermal conductivity at various magnitudes of the top wall temperature (right).

proposed model for a few thermal and compressible flows. The setups chosen are the Sod shock tube, a common test for the accuracy of compressible solvers, the thermoacoustic convection, which has the presence of various timescales and length scales, and the Rayleigh-Bénard convection, a standard test case for thermal flows [41].

**A. Sod shock tube**

We study the time evolution of a one-dimensional front in Sod’s shock tube. This is considered a standard test case to check the accuracy and stability of compressible flow solvers. The setup consists of an initially quiescent fluid in the two regions  $L$  and  $R$ . The two regions located in  $x = -0.5$  to  $0$  and  $x = 0$  to  $0.5$ , respectively, are separated by an interface at  $x = 0$  across which the density and pressure have a jump

$$\begin{pmatrix} \rho_L \\ u_L \\ p_L \end{pmatrix} = \begin{pmatrix} 1 \\ 0 \\ 1 \end{pmatrix}, \quad \begin{pmatrix} \rho_R \\ u_R \\ p_R \end{pmatrix} = \begin{pmatrix} 0.125 \\ 0 \\ 0.1 \end{pmatrix}. \quad (69)$$

The presence of a sharp discontinuity in the initial condition at the center of the domain generates a moving compressive shock front in the low density region and rarefaction front in the high density region. These two fronts leave behind in the tube a central contact region of uniform pressure and velocity [86].

Here, for the test case we consider the reference viscosity  $\mu = 10^{-5}$ . The simulations were performed on a coarse grid  $A$  of size  $500 \times 8 \times 8$ , and a refined grid  $B$  of size  $2000 \times 8 \times 8$ . The periodic boundary conditions were implemented in  $(y, z)$ -normal directions and standard bounce back in  $x$ -normal direction. The timescale is chosen based on the length

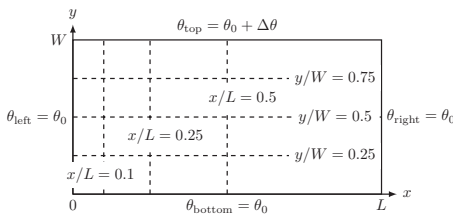


FIG. 10. Sketch representing the geometry of the two-dimensional box and the imposed wall temperatures.

of the domain and speed of sound in the right section of the domain. The simulations were run until the nondimensional time  $t^* = 0.2$ , that is earlier than either of the fronts hit the wall.

Figure 13 contrasts the density, pressure, and velocity obtained from the present model with those from the direct integration of Navier-Stokes-Fourier equations. Simulations on the coarse grid show oscillations in the region of discontinuity. The contact region shows a very minute jump in the pressure and there exists a small discrepancy in velocity at the tail of the expansion front. It is evident that the speed of the shock is captured accurately by the model.

**B. Thermoacoustic convection**

Thermoacoustic convection refers to the convective currents set up in a compressible fluid due to rapid heating of one of the walls [87–89]. It manifests in the form of a pressure wave initiated at the heated wall that is reflected back and forth in the domain until it gets dissipated by viscosity. The thermally induced motion is known to enhance the heat transfer relative to pure conduction by addition of a convective mode [87]. As the steady state is attained, the convective mode gradually dissipates and conduction becomes the dominant mode of heat transfer [90]. The numerical modeling of thermoacoustic phenomenon is considered a challenging problem due to the presence of multiple timescales and length scales.

The simulation setup consists of a grid of size  $8 \times 128 \times 8$  with  $\theta_{hot} = 1.01\theta_0$ ,  $\theta_{cold} = \theta_0$ , and  $u_{top} = u_{bottom} = 0$ . The viscosity is calculated from the Knudsen number  $Kn = 10^{-4}$ . To benchmark the results, the compressible Navier-Stokes-Fourier (NSF) were solved using the scheme of Ref. [87] subjected to the boundary conditions

$$\begin{aligned} u(y = 0, t) &= u(y = H, t) = 0, \\ \theta(y = H, t) &= \theta_{hot}, \\ \theta(y = 0, t) &= \theta_{cold}, \end{aligned} \quad (70)$$

and initial condition  $\rho(y, t = 0) = \rho_0$ ,  $u(y, t = 0) = 0$ , and  $\theta(y, t = 0) = \theta_{cold}$ . Figure 14 compares the temperature, density, and pressure profile obtained from the  $RD3Q67$  simulations with solution to NSF equations and they are found to be in agreement. This suggests that the current model is well suited for studying the various compressible flows.

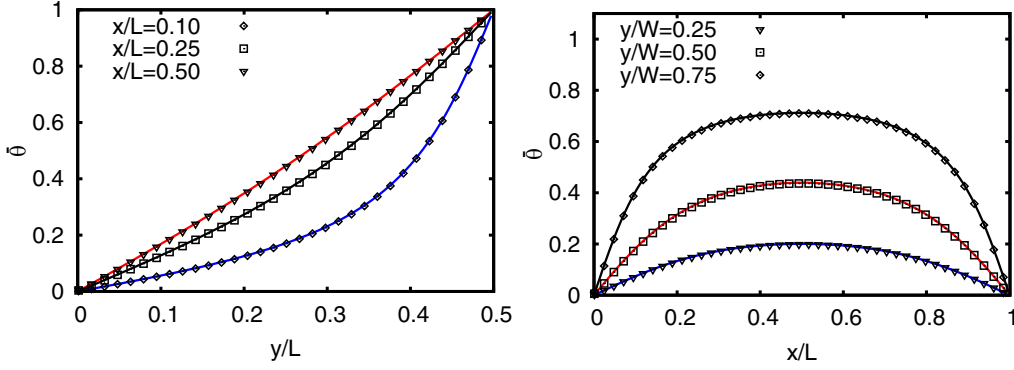


FIG. 11. Steady-state conduction in a two-dimensional plate: temperature plots along constant  $x$  lines (left) and along constant  $y$  lines (right). The solid lines are the analytical solution of the conduction equation while the symbols are from simulations.

### C. Rayleigh-Bénard convection

Rayleigh-Bénard convection is considered a classical benchmark on the thermal models [23]. The setup consists of a horizontal layer of viscous fluid confined between two thermally well conducting parallel plates kept at a distance  $L$ . The bottom plate is at an excess temperature  $\theta_{\text{bottom}}$ , while the top plate is maintained at a lower temperature  $\theta_{\text{top}}$ . The flow is caused by the temperature induced unstable density gradients in the presence of external force field (usually gravitational field).

The dynamics is characterized by nondimensional parameter Rayleigh number ( $Ra$ ), that represents the strength of buoyancy driven inertial force to the viscous force and is defined as

$$Ra = \frac{g\hat{\beta}\Delta\theta L^3}{\nu\alpha_T}, \quad (71)$$

where  $g$  is the gravity in the negative  $y$  direction,  $\hat{\beta} = -1/\rho(\partial\rho/\partial T)_P$  is the thermal expansion coefficient,  $\Delta\theta$  is the temperature difference between the two walls,  $\nu$  is the kinematic viscosity, and  $\alpha_T$  is the thermal diffusivity. Below a certain critical Rayleigh number ( $Ra_c \approx 1708$ ) where the heat transfer is entirely conductive in nature, a steady solution exists with the velocity zero everywhere and the temperature a linear function of the vertical coordinate

$$\theta = \theta_{\text{bottom}} - \Delta\theta \frac{y}{L}. \quad (72)$$

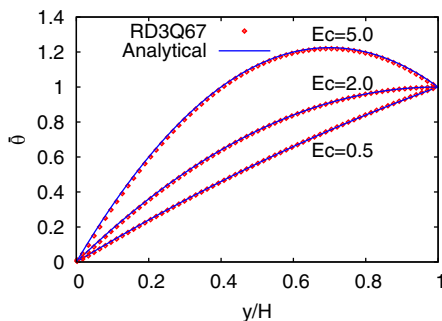


FIG. 12. Mean planar temperature profiles obtained from RD3Q67 at steady state compared against the analytical solution.

However, when  $Ra$  is increased above the critical value, this solution becomes unstable to small disturbances and the convection currents are set up. As  $Ra$  is increased further, the flow becomes turbulent in nature.

The gravitational force is incorporated in the collision step via a forcing term  $F_i$ . The update of populations is written as

$$\begin{aligned} f_i(\mathbf{x} + \mathbf{c}_i \Delta t, t + \Delta t) &= f_i(\mathbf{x}, t) + \alpha\beta [f_i^{\text{eq}}(\rho, \hat{\mathbf{u}}, \hat{\theta}) - f_i(\mathbf{x}, t)] \\ &+ \left(1 - \frac{\alpha\beta}{2}\right) \Delta t F_i, \end{aligned} \quad (73)$$

where

$$\hat{\mathbf{u}} = \frac{1}{\rho} \langle f, \mathbf{c} \rangle + \frac{\Delta t}{2} \mathbf{g}, \quad \hat{\theta} = \frac{1}{3\rho} (\langle f, \mathbf{c}^2 \rangle - \rho \hat{\mathbf{u}}^2), \quad (74)$$

and  $\alpha = 2$  is the single relaxation time standard LBM. For high  $Ra$ ,  $\alpha$  needs to be computed from the entropic formulation of LBM [64]. The force term is

$$F_i = \frac{\rho w_i \mathbf{c}_i \cdot \mathbf{g}}{\theta_0}. \quad (75)$$

Here, it should be pointed that the alternate ways to evaluate the hydrodynamic moments involve averaging the moments before and after collision [91] or shifting them [68], and are subject of further research for the proposed model.

The numerical simulations were carried on a grid size of  $256 \times 128 \times 8$  with  $\theta_{\text{bottom}} = 1.05\theta_0$  and  $\theta_{\text{top}} = 0.95\theta_0$ . Constant temperature boundary conditions at the top and the bottom walls were imposed and periodic boundary conditions were applied in the other two directions. Following Refs. [24,29], the setup was initialized with a sinusoidal perturbation of the temperature field and left to evolve until two diffusion times. However, any random initial perturbation provided to the system triggers the instability. The Nusselt number and the temperature contours at the steady state are independent of the initial perturbation provided to the system. At  $Ra > 10^6$  for this setup,  $\alpha$  was recomputed from the entropic formulation of LBM to suppress the disruptive numerical instabilities [64]. Figure 15 depicts the isotherm contours for 2D Rayleigh-Bénard convection at various  $Ra$ . Figure 16 visualizes the temperature field for 3D Rayleigh-

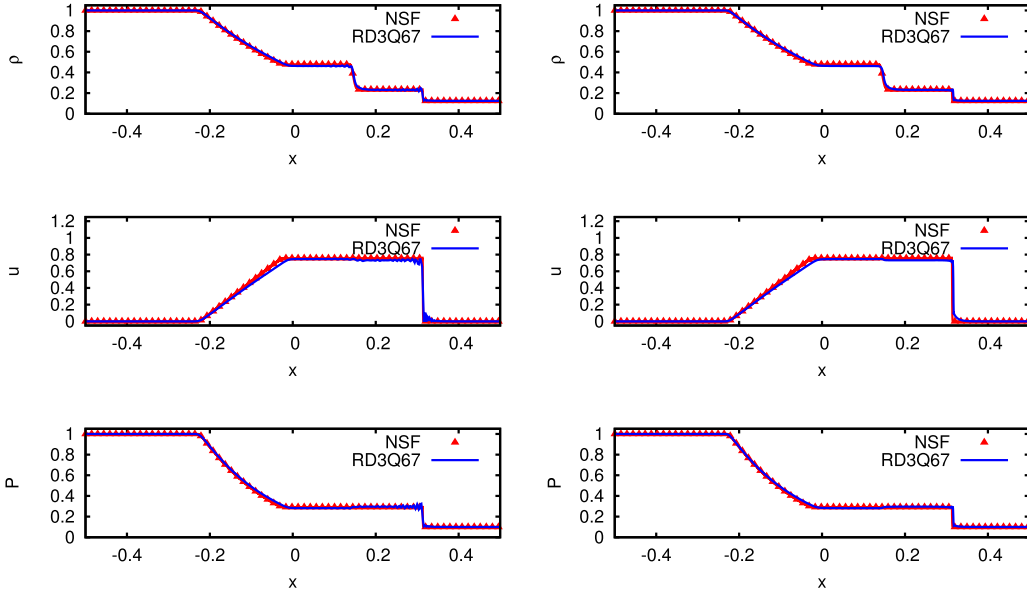


FIG. 13. The figure shows the variation of density ( $\rho$ ), velocity ( $u$ ), and pressure ( $P$ ) along the tube for the Sod's shock test. The figure contrasts  $RD3Q67$  simulation results from runs  $A$  (left) and  $B$  (right) with NSF equations at  $t^* = 0.2$ .

Bénard convection at a grid size of  $1024 \times 512 \times 1024$  at  $Ra = 10^9$ . For quantitative analysis, we calculate the Nusselt number ( $Nu$ ) which is the measure of heat transfer in the system and represents the ratio of net heat transfer to the

conductive heat transfer

$$Nu = 1 + \frac{\langle u_y \tilde{\theta} \rangle}{\alpha_T \Delta \theta / H}, \quad (76)$$

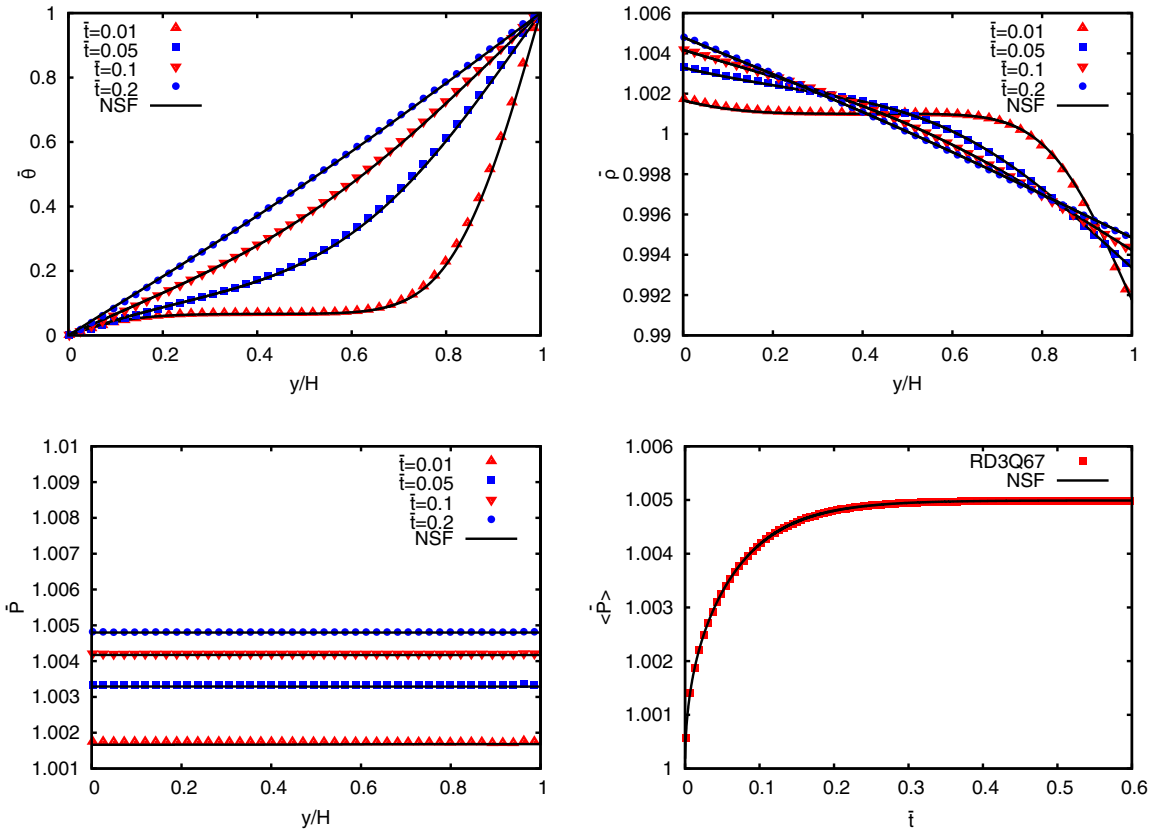


FIG. 14. Normalized temperature  $\tilde{\theta} = (\theta - \theta_{\text{cold}})/(\theta_{\text{hot}} - \theta_{\text{cold}})$ , density  $\tilde{\rho} = \rho/\rho_0$ , pressure  $\tilde{P} = \rho\theta/(\rho_0\theta_{\text{cold}})$ , and volume averaged pressure ( $\tilde{P}$ ) profiles for thermoacoustic convection at various times. Here,  $\tilde{t} = t\nu/H^2$ . The symbols are obtained from simulation while the lines are from the solution to the NSF equations.

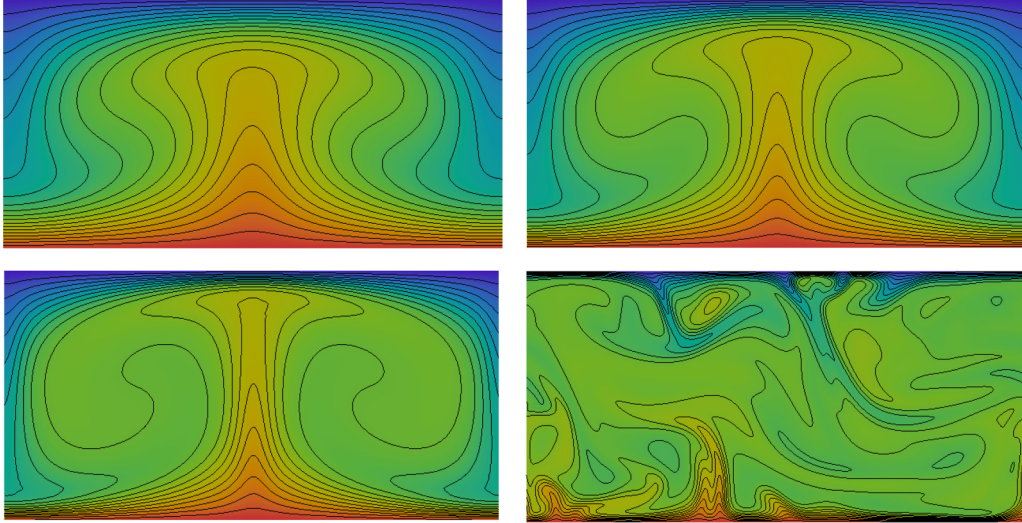


FIG. 15. Temperature field for the Rayleigh-Bénard convection at  $Ra = 1.0 \times 10^4$  (top left),  $3.0 \times 10^4$  (top right),  $1.5 \times 10^5$  (bottom left),  $1.0 \times 10^7$  (bottom right). The lines represent isotherm contours of temperature normalized from 0 to 1 in steps of 0.05.

where  $\alpha_T$  is the thermal diffusivity, and  $\langle \cdot \rangle$  represents average over the entire domain of flow. Here,  $\hat{\theta} = \hat{\theta} - (\theta_{\text{bottom}} - \Delta\theta y/L)$  is the deviation from the temperature distribution in the static state [92,93]. In Fig. 17, the Nusselt number obtained from current simulations is compared with that from Ref. [93] and the empirical power law  $Nu = 1.56(Ra/Ra_{cr})^{0.296}$ . In Fig. 18, a grid convergence study is performed at  $Ra = 10^4$ , and is found to reveal second-order convergence of the scheme. To test the accuracy of the model at large temperature deviations, a Rayleigh-Bénard simulation at  $Ra = 10^4$  on a grid size of  $256 \times 128 \times 8$  with top wall temperature  $0.5\theta_0$  and bottom wall temperature  $1.5\theta_0$  was performed. The Nusselt number obtained was 2.6797, whereas the Nusselt number for wall temperatures  $(1 \pm 0.05)\theta_0$  was 2.6426 while the empirical power law suggests the Nusselt number to be 2.6321. Hence, the 50% temperature run gave an error of 1.8% whereas the 5% temperature deviation gave an error of only 0.4%. This suggests that the accuracy of the model is not compromised at large temperature deviations. A detailed quantitative analysis of high  $Ra$  convection has been kept out of the scope of this paper.

## XII. OUTLOOK

In this paper, we have presented an energy conserving lattice Boltzmann model based on a single set of populations. It exhibits accurate thermohydrodynamic behavior with a high degree of accuracy and is therefore capable of simulating compressible and thermal hydrodynamics. The theoretical requirements and the methodology to construct this model have been described in detail and can be employed to construct even more accurate models. Several test cases were simulated using the proposed model and it was found to be nonlinearly stable for a wide range of parameters. The test cases confirmed that the model correctly captures viscous heating, shocks, heat conduction, and compressible hydrodynamics. The test case of thermoacoustic convection clearly proves excellent agreement with the NSF equations at the diffusive timescales. Some preliminary studies have shown that it also reproduces correct behavior at acoustic timescales, which is a subject of further research. As the model is nonlinearly stable, it opens the possibility to study turbulent thermal flows such as the turbulent Rayleigh-Bénard convection. The limitation on the Prandtl number is due to the BGK collision model and can be addressed by using quasiequilibrium models [94,95].

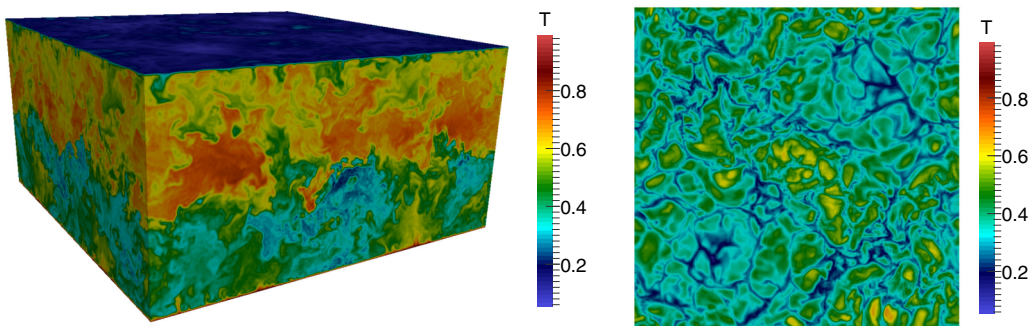


FIG. 16. Rayleigh Bénard convection at  $Ra = 10^9$ : temperature field at the boundaries (left) and on a horizontal slice close to the top wall (right).

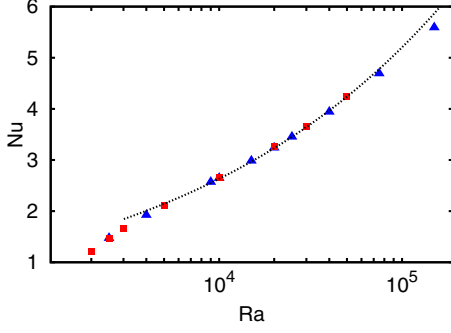


FIG. 17. Nu vs Ra, triangles are from current simulation, squares are from Ref. [93], line is empirical power law  $Nu = 1.56(Ra/Ra_c)^{0.296}$ .

### APPENDIX: EVOLUTION OF THE THERMOHYDRODYNAMIC MOMENTS

We begin with the Boltzmann BGK equation

$$\partial_t f + \partial_\beta (f c_\beta) = \Omega(f), \quad (\text{A1})$$

where  $\Omega(f) = (f^{\text{eq}} - f)/\tau$  is the collision kernel, with  $\tau$  as the relaxation time. We define the peculiar velocity  $\xi_\alpha = c_\alpha - u_\alpha$ , and the integral

$$\int f \psi(\xi) d\xi = \langle f, \psi(\xi) \rangle. \quad (\text{A2})$$

The various moments can be found as

$$\begin{aligned} & \langle f, \{1, \xi_\alpha, \xi_\alpha \xi_\beta, \frac{1}{2} \xi^2, \xi_\alpha \xi_\beta \xi_\gamma, \frac{1}{2} \xi^2 \xi_\alpha, \xi^2 \xi_\alpha \xi_\beta, \xi^4\} \rangle \\ & = \{1, 0, p \delta_{\alpha\beta} + \sigma_{\alpha\beta}, \frac{3}{2} p, Q_{\alpha\beta\gamma}, q_\alpha, R_{\alpha\beta}, R\}. \end{aligned} \quad (\text{A3})$$

The traceless part  $\overline{A_{\alpha\beta}}$  of any second-order tensor  $A_{\alpha\beta}$  is defined as

$$\overline{A_{\alpha\beta}} = \frac{1}{2}(A_{\alpha\beta} + A_{\beta\alpha} - \frac{2}{3} A_{\gamma\gamma} \delta_{\alpha\beta}). \quad (\text{A4})$$

We also define

$$\overline{Q_{\alpha\beta\gamma}} = Q_{\alpha\beta\gamma} - \frac{2}{5}(q_\alpha \delta_{\beta\gamma} + q_\beta \delta_{\alpha\gamma} + q_\gamma \delta_{\alpha\beta}) \quad (\text{A5})$$

and

$$\overline{R_{\alpha\beta}} = R_{\alpha\beta} - \frac{1}{3} R \delta_{\alpha\beta}. \quad (\text{A6})$$

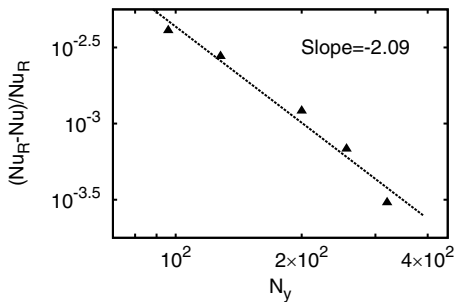


FIG. 18. Grid convergence study for  $Ra = 10^4$  reveals second-order convergence. The converged  $Nu_R$  is 2.6311 with 360 points in the vertical direction. The line is the fitted curve.

Multiplying Eq. (A1) with  $\phi(\xi)$  one obtains

$$\begin{aligned} & \partial_t \langle f \phi(\xi) \rangle - \langle f, \partial_t \phi(\xi) \rangle + \partial_\beta \langle f c_\beta \phi(\xi) \rangle - \langle f c_\beta, \partial_\beta \phi(\xi) \rangle \\ & = \Omega \langle f \phi(\xi) \rangle. \end{aligned} \quad (\text{A7})$$

Applying the chain rule and integrating over the velocity space one obtains

$$\begin{aligned} & \partial_t \langle f, \phi(\xi) \rangle - \langle f, (\partial_t \xi_\alpha) \partial_{\xi_\alpha} \phi(\xi) \rangle + \partial_\beta \langle f, (\xi_\beta + u_\beta) \phi(\xi) \rangle \\ & - \langle f, c_\beta (\partial_\beta \xi_\alpha) \partial_{\xi_\alpha} \phi(\xi) \rangle = \langle \Omega(f), \phi(\xi) \rangle. \end{aligned} \quad (\text{A8})$$

Now, substituting  $\partial_t \xi_\alpha = \partial_t (c_\alpha - u_\alpha) = -\partial_t u_\alpha$  and  $\partial_\beta \xi_\alpha = \partial_\beta (c_\alpha - u_\alpha) = -\partial_\beta u_\alpha$  we get

$$\begin{aligned} & \partial_t \langle f, \phi(\xi) \rangle + (\partial_t u_\alpha) \langle f, \partial_{\xi_\alpha} \phi(\xi) \rangle \\ & + \partial_\beta \langle f, \xi_\beta \phi(\xi) \rangle + \partial_\beta [u_\beta \langle f, \phi(\xi) \rangle] \\ & + (\partial_\beta u_\alpha) \langle f, c_\beta \partial_{\xi_\alpha} \phi(\xi) \rangle = \langle \Omega(f), \phi(\xi) \rangle. \end{aligned} \quad (\text{A9})$$

#### 1. Evolution of density

Substituting  $\phi(\xi) = 1$  in Eq. (A9) we obtain the evolution of density (the continuity equation) as

$$\partial_t \rho + 0 + 0 + \partial_\alpha (\rho u_\alpha) + 0 = 0. \quad (\text{A10})$$

#### 2. Evolution of velocity

Substituting  $\phi(\xi) = \xi_\gamma$  in Eq. (A9) we obtain the evolution of velocity as

$$0 + \partial_t u_\gamma + \frac{1}{\rho} \partial_\beta (p \delta_{\gamma\beta} + \sigma_{\gamma\beta}) + 0 + u_\beta \partial_\beta u_\gamma = 0. \quad (\text{A11})$$

#### 3. Evolution of pressure, temperature, and the stress tensor

Substituting  $\phi(\xi) = \xi_\gamma \xi_\kappa$  in Eq. (A9) we obtain

$$\begin{aligned} & \partial_t [p \delta_{\gamma\kappa} + \sigma_{\gamma\kappa}] + 0 + \partial_\beta Q_{\beta\gamma\kappa} + \partial_\beta [u_\beta (p \delta_{\gamma\kappa} + \sigma_{\gamma\kappa})] \\ & + (\partial_\beta u_\alpha) \langle f, c_\beta (\xi_\kappa \delta_{\alpha\gamma} + \xi_\gamma \delta_{\alpha\kappa}) \rangle \\ & = \frac{1}{\tau} (\sigma_{\gamma\kappa}^{\text{eq}} - \sigma_{\gamma\kappa}). \end{aligned} \quad (\text{A12})$$

Substituting  $c_\beta = \xi_\beta + u_\beta$  and integrating further we obtain

$$\begin{aligned} & \partial_t [p \delta_{\gamma\kappa} + \sigma_{\gamma\kappa}] + \partial_\beta Q_{\beta\gamma\kappa} + \partial_\beta [u_\beta (p \delta_{\gamma\kappa} + \sigma_{\gamma\kappa})] \\ & + (p \delta_{\beta\kappa} + \sigma_{\beta\kappa}) \partial_\beta u_\gamma + (p \delta_{\beta\gamma} + \sigma_{\beta\gamma}) \partial_\beta u_\kappa \\ & = \frac{1}{\tau} (\sigma_{\gamma\kappa}^{\text{eq}} - \sigma_{\gamma\kappa}). \end{aligned} \quad (\text{A13})$$

Taking the trace (i.e., multiply with  $\delta_{\gamma\kappa}$ ) of the above equation we obtain

$$3 \partial_t p + 3 u_\beta \partial_\beta p + 5 p \partial_\beta u_\beta + 2 \partial_\beta q_\beta + 2 \sigma_{\beta\kappa} \partial_\beta u_\kappa = 0, \quad (\text{A14})$$

which gives the evolution of pressure as

$$\partial_t p + u_\beta \partial_\beta p + \frac{5}{3} p \partial_\beta u_\beta + \frac{2}{3} \sigma_{\beta\gamma} \partial_\beta u_\gamma + \frac{2}{3} \partial_\beta q_\beta = 0. \quad (\text{A15})$$

Substituting  $p = \rho\theta$  in the evolution of pressure and rearranging the terms one obtains

$$\partial_t \theta + u_\beta \partial_\beta \theta + \frac{2}{3} \theta \partial_\beta u_\beta + \frac{2}{3\rho} \sigma_{\beta\gamma} \partial_\beta u_\gamma + \frac{2}{3\rho} \partial_\beta q_\beta + \theta [\partial_t \rho + \partial_\beta (\rho u_\beta)] = 0, \quad (\text{A16})$$

where the term in square brackets is zero because of Eq. (A10). Therefore, we obtain the evolution of temperature as

$$\partial_t \theta + u_\beta \partial_\beta \theta + \frac{2}{3} \theta \partial_\beta u_\beta + \frac{2}{3\rho} \sigma_{\beta\gamma} \partial_\beta u_\gamma + \frac{2}{3\rho} \partial_\beta q_\beta = 0. \quad (\text{A17})$$

Multiplying Eq. (A15) with  $\delta_{\gamma\kappa}$  and subtracting from Eq. (A13) one obtains

$$\begin{aligned} & \partial_t [p \delta_{\gamma\kappa} + \sigma_{\gamma\kappa}] + \partial_\beta Q_{\beta\gamma\kappa} + \partial_\beta [u_\beta (p \delta_{\gamma\kappa} + \sigma_{\gamma\kappa})] + (p \delta_{\beta\kappa} + \sigma_{\beta\kappa}) \partial_\beta u_\gamma + (p \delta_{\beta\gamma} + \sigma_{\beta\gamma}) \partial_\beta u_\kappa \\ & - \left[ \partial_t p + u_\beta \partial_\beta p + \frac{5}{3} p \partial_\beta u_\beta + \frac{2}{3} \sigma_{\beta\gamma} \partial_\beta u_\gamma + \frac{2}{3} \partial_\beta q_\beta \right] \delta_{\gamma\kappa} = \frac{1}{\tau} (\sigma_{\gamma\kappa}^{\text{eq}} - \sigma_{\gamma\kappa}), \end{aligned} \quad (\text{A18})$$

which can be simplified as

$$\begin{aligned} & \partial_t \sigma_{\gamma\kappa} + \partial_\beta [u_\beta \sigma_{\gamma\kappa}] + \partial_\beta Q_{\beta\gamma\kappa} - \frac{2}{3} \delta_{\gamma\kappa} \partial_\beta q_\beta + p \partial_\kappa u_\gamma + p \partial_\gamma u_\kappa - \frac{2}{3} p \delta_{\gamma\kappa} \partial_\beta u_\beta + \sigma_{\beta\kappa} \partial_\beta u_\gamma + \sigma_{\beta\gamma} \partial_\beta u_\kappa \\ & - \frac{2}{3} \delta_{\gamma\kappa} \sigma_{\beta\gamma} \partial_\beta u_\gamma = \frac{1}{\tau} (\sigma_{\gamma\kappa}^{\text{eq}} - \sigma_{\gamma\kappa}). \end{aligned} \quad (\text{A19})$$

Rearranging the terms in the above equation we obtain the evolution of the stress tensor as

$$\partial_t \sigma_{\alpha\beta} + u_\gamma \partial_\gamma \sigma_{\alpha\beta} + \partial_\gamma \overline{Q_{\alpha\beta\gamma}} + \sigma_{\alpha\beta} \partial_\gamma u_\gamma + 2 \overline{\sigma_{\gamma\beta} \partial_\gamma u_\alpha} + 2 p \overline{\partial_\beta u_\alpha} + \frac{4}{5} \overline{\partial_\beta q_\alpha} = \frac{1}{\tau} (\sigma_{\alpha\beta}^{\text{eq}} - \sigma_{\alpha\beta}). \quad (\text{A20})$$

#### 4. Evolution of the heat flux

Substituting  $\phi(\xi) = \xi^2 \xi_\alpha / 2$  in Eq. (A9) we obtain

$$\begin{aligned} & \partial_t q_\alpha + (\partial_t u_\beta) \left[ \frac{5}{2} p \delta_{\alpha\beta} + \sigma_{\alpha\beta} \right] + \frac{1}{2} \partial_\beta R_{\alpha\beta} + \partial_\beta (q_\alpha u_\beta) + (\partial_\beta u_\alpha) \left\langle f, \frac{1}{2} \xi^2 (\xi_\beta + u_\beta) \right\rangle \\ & + (\partial_\beta u_\gamma) \langle f, \xi_\alpha \xi_\gamma (\xi_\beta + u_\beta) \rangle = \frac{1}{\tau} (q_\alpha^{\text{eq}} - q_\alpha), \end{aligned} \quad (\text{A21})$$

which after substituting  $\partial_t u_\beta$  from Eq. (A11) is further simplified as

$$\begin{aligned} & \partial_t q_\alpha - \left( u_\kappa \partial_\kappa u_\beta + \frac{1}{\rho} \partial_\beta p + \frac{1}{\rho} \partial_\kappa \sigma_{\beta\kappa} \right) \left[ \frac{5}{2} p \delta_{\alpha\beta} + \sigma_{\alpha\beta} \right] + q_\beta \partial_\beta u_\alpha + \frac{1}{2} \partial_\beta R_{\alpha\beta} + \partial_\beta (q_\alpha u_\beta) + Q_{\alpha\beta\gamma} \partial_\beta u_\gamma \\ & + \frac{3}{2} p u_\beta \partial_\beta u_\alpha + u_\beta (p \delta_{\alpha\gamma} + \sigma_{\alpha\gamma}) (\partial_\beta u_\gamma) = \frac{1}{\tau} (q_\alpha^{\text{eq}} - q_\alpha), \end{aligned} \quad (\text{A22})$$

where upon rearranging the terms we obtain the evolution for heat flux as

$$\begin{aligned} & \partial_t q_\alpha + \frac{1}{2} \partial_\beta \left( \overline{R_{\alpha\beta}} + \frac{1}{3} R \delta_{\alpha\beta} \right) + \overline{Q_{\alpha\beta\gamma}} \partial_\gamma u_\beta + \partial_\beta (q_\alpha u_\beta) + \frac{7}{5} q_\beta \partial_\beta u_\alpha + \frac{2}{5} q_\alpha \partial_\beta u_\beta + \frac{2}{5} q_\beta \partial_\alpha u_\beta \\ & - \frac{5}{2} \frac{p}{\rho} \partial_\alpha p - \frac{\sigma_{\alpha\beta}}{\rho} \partial_\beta p - \frac{5}{2} \frac{p}{\rho} \partial_\theta \sigma_{\alpha\theta} - \frac{\sigma_{\alpha\beta}}{\rho} \partial_\theta \sigma_{\beta\theta} = \frac{1}{\tau} (q_\alpha^{\text{eq}} - q_\alpha). \end{aligned} \quad (\text{A23})$$

- 
- |   |   |
|---|---|
| [1] S. Succi, <i>The Lattice Boltzmann Equation: for Fluid Dynamics and Beyond</i> (Oxford University Press, Oxford, 2001). | [6] S. P. Thampi, R. Golestanian, and J. M. Yeomans, <i>Phys. Rev. Lett.</i> <b>111</b> , 118101 (2013).                            |
| [2] S. Chen and G. D. Doolen, <i>Annu. Rev. Fluid Mech.</i> <b>30</b> , 329 (1998).   | [7] M. Mendoza, B. M. Boghosian, H. J. Herrmann, and S. Succi, <i>Phys. Rev. Lett.</i> <b>105</b> , 014502 (2010).                  |
| [3] C. K. Aidun and J. R. Clausen, <i>Annu. Rev. Fluid Mech.</i> <b>42</b> , 439 (2010).                                    | [8] R. Benzi, M. Bernaschi, M. Sbragaglia, and S. Succi, <i>Europhys. Lett.</i> <b>104</b> , 48006 (2013).                          |
| [4] C. Thantapanally, D. V. Patil, S. Succi, and S. Ansumali, <i>J. Fluid Mech.</i> <b>728</b> , R4 (2013).                 | [9] H. Chen, S. A. Orszag, I. Staroselsky, and S. Succi, <i>J. Fluid Mech.</i> <b>519</b> , 301 (2004).                             |
| [5] S. Singh, G. Subramanian, and S. Ansumali, <i>Phys. Rev. E</i> <b>88</b> , 013301 (2013).                               | [10] S. Ansumali, I. V. Karlin, S. Arcidiacono, A. Abbas, and N. I. Prasianakis, <i>Phys. Rev. Lett.</i> <b>98</b> , 124502 (2007). |

- [11] H. Chen, S. Chen, and W. H. Matthaeus, *Phys. Rev. A* **45**, R5339 (1992).
- [12] Y. H. Qian, D. d'Humières, and P. Lallemand, *Europhys. Lett.* **17**, 479 (1992).
- [13] P. Lallemand and L. S. Luo, *Phys. Rev. E* **61**, 6546 (2000).
- [14] R. Benzi, S. Succi, and M. Vergassola, *Phys. Rep.* **222**, 145 (1992).
- [15] F. J. Higuera, S. Succi, and R. Benzi, *Europhys. Lett.* **9**, 345 (1989).
- [16] S. Succi, I. V. Karlin, and H. Chen, *Rev. Mod. Phys.* **74**, 1203 (2002).
- [17] M. Namburi, S. Krithivasan, and S. Ansumali, *Sci. Rep.* **6**, 27172 (2016).
- [18] W. P. Yudistiawan, S. K. Kwak, D. V. Patil, and S. Ansumali, *Phys. Rev. E* **82**, 046701 (2010).
- [19] A. J. C. Ladd, *Phys. Rev. Lett.* **70**, 1339 (1993).
- [20] R. Adhikari, K. Stratford, M. E. Cates, and A. J. Wagner, *Europhys. Lett.* **71**, 473 (2005).
- [21] S. S. Chikatamarla, C. E. Frouzakis, I. V. Karlin, A. G. Tomboulides, and K. B. Boulouchos, *J. Fluid Mech.* **656**, 298 (2010).
- [22] A. Bartoloni, C. Battista, S. Cabasino, P. Paolucci, J. Pech, R. Sarno, G. Todesco, M. Torelli, W. Tross, P. Vicini *et al.*, *Int. J. Mod. Phys. C* **04**, 993 (1993).
- [23] X. Shan, *Phys. Rev. E* **55**, 2780 (1997).
- [24] X. He, S. Chen, and G. D. Doolen, *J. Comput. Phys.* **146**, 282 (1998).
- [25] F. J. Alexander, S. Chen, and J. D. Sterling, *Phys. Rev. E* **47**, R2249 (1993).
- [26] G. R. McNamara, A. L. Garcia, and B. J. Alder, *J. Stat. Phys.* **87**, 1111 (1997).
- [27] S. S. Chikatamarla and I. V. Karlin, *Phys. Rev. E* **79**, 046701 (2009).
- [28] R. Ramadugu, S. P. Thampi, R. Adhikari, S. Succi, and S. Ansumali, *Europhys. Lett.* **101**, 50006 (2013).
- [29] I. V. Karlin, D. Sichau, and S. S. Chikatamarla, *Phys. Rev. E* **88**, 063310 (2013).
- [30] Y. Feng, P. Sagaut, and W. Tao, *J. Comput. Phys.* **303**, 514 (2015).
- [31] G. Pareschi, N. Frapolli, S. S. Chikatamarla, and I. V. Karlin, *Phys. Rev. E* **94**, 013305 (2016).
- [32] G. G. Pereira, B. Wu, and S. Ahmed, *Phys. Rev. E* **96**, 063108 (2017).
- [33] Y. Peng, C. Shu, and Y. T. Chew, *Phys. Rev. E* **68**, 026701 (2003).
- [34] S. S. Chikatamarla, S. Ansumali, and I. V. Karlin, *Phys. Rev. Lett.* **97**, 010201 (2006).
- [35] T. Abe, *J. Comput. Phys.* **131**, 241 (1997).
- [36] X. He and L. S. Luo, *Phys. Rev. E* **55**, R6333 (1997).
- [37] X. He and L. S. Luo, *Phys. Rev. E* **56**, 6811 (1997).
- [38] X. Shan and X. He, *Phys. Rev. Lett.* **80**, 65 (1998).
- [39] S. Ansumali, I. V. Karlin, and H. C. Öttinger, *Europhys. Lett.* **63**, 798 (2003).
- [40] B. Dorschner, F. Bösch, and I. V. Karlin, *Phys. Rev. Lett.* **121**, 130602 (2018).
- [41] N. Frapolli, S. S. Chikatamarla, and I. V. Karlin, *Phys. Rev. E* **90**, 043306 (2014).
- [42] N. Frapolli, S. S. Chikatamarla, and I. V. Karlin, *Phys. Rev. E* **92**, 061301 (2015).
- [43] S. Ansumali and I. V. Karlin, *Phys. Rev. Lett.* **95**, 260605 (2005).
- [44] C. Cercignani, *The Boltzmann Equation and Its Applications* (Springer, New York, 1988).
- [45] R. L. Liboff, *Kinetic Theory: Classical, Quantum, and Relativistic Descriptions* (Springer, New York, 2003).
- [46] P. L. Bhatnagar, E. P. Gross, and M. Krook, *Phys. Rev.* **94**, 511 (1954).
- [47] J. L. Lebowitz, H. L. Frisch, and E. Helfand, *Phys. Fluids* **3**, 325 (1960).
- [48] R. Monaco and L. Preziosi, *Fluid Dynamic Applications of the Discrete Boltzmann Equation*, Vol. 3 (World Scientific, Singapore, 1991).
- [49] J. E. Broadwell, *Phys. Fluids* **7**, 1243 (1964).
- [50] S. Chapman and T. G. Cowling, *The Mathematical Theory of Non-uniform Gases* (Cambridge University Press, Cambridge, 1970).
- [51] A. G. Shet, S. H. Sorathiya, S. Krithivasan, A. M. Deshpande, B. Kaul, S. D. Sherlekar, and S. Ansumali, *Phys. Rev. E* **88**, 013314 (2013).
- [52] A. J. Wagner, *Europhys. Lett.* **44**, 144 (1998).
- [53] I. V. Karlin, A. Ferrante, and H. C. Öttinger, *Europhys. Lett.* **47**, 182 (1999).
- [54] V. Sofonea, *Phys. Rev. E* **74**, 056705 (2006).
- [55] V. E. Ambruş and V. Sofonea, *Phys. Rev. E* **86**, 016708 (2012).
- [56] N. Frapolli, S. S. Chikatamarla, and I. V. Karlin, *Phys. Rev. Lett.* **117**, 010604 (2016).
- [57] S. Ansumali and I. V. Karlin, *Phys. Rev. E* **62**, 7999 (2000).
- [58] B. M. Boghosian, J. Yepez, P. V. Coveney, and A. J. Wagner, *Proc. R. Soc. London, Ser. A* **457**, 717 (2001).
- [59] S. Ansumali and I. V. Karlin, *J. Stat. Phys.* **107**, 291 (2002).
- [60] F. Tosi, S. Ubertini, S. Succi, and I. V. Karlin, *J. Sci. Comput.* **30**, 369 (2006).
- [61] S. Ansumali and I. V. Karlin, *Phys. Rev. E* **65**, 056312 (2002).
- [62] A. N. Gorban and D. Packwood, *Phys. Rev. E* **86**, 025701 (2012).
- [63] R. A. Brownlee, A. N. Gorban, and J. Levesley, *Phys. Rev. E* **75**, 036711 (2007).
- [64] M. Atif, P. K. Kolluru, C. Thantapanally, and S. Ansumali, *Phys. Rev. Lett.* **119**, 240602 (2017).
- [65] Y. H. Qian and Y. Zhou, *Europhys. Lett.* **42**, 359 (1998).
- [66] G. Vahala, P. Pavlo, L. Vahala, and N. S. Martys, *Int. J. Mod. Phys. C* **09**, 1247 (1998).
- [67] S. S. Chikatamarla and I. V. Karlin, *Phys. Rev. Lett.* **97**, 190601 (2006).
- [68] M. Sbragaglia, R. Benzi, L. Biferale, H. Chen, X. Shan, and S. Succi, *J. Fluid Mech.* **628**, 299 (2009).
- [69] X. Shan, *Phys. Rev. E* **81**, 036702 (2010).
- [70] I. V. Karlin, A. N. Gorban, S. Succi, and V. Boffi, *Phys. Rev. Lett.* **81**, 6 (1998).
- [71] B. M. Boghosian, P. J. Love, P. V. Coveney, I. V. Karlin, S. Succi, and J. Yepez, *Phys. Rev. E* **68**, 025103 (2003).
- [72] H. Chen and C. Teixeira, *Comp. Phys. Commun.* **129**, 21 (2000).
- [73] B. Dorschner, F. Bösch, S. S. Chikatamarla, K. Boulouchos, and I. V. Karlin, *J. Fluid Mech.* **801**, 623 (2016).
- [74] B. Dorschner, N. Frapolli, S. S. Chikatamarla, and I. V. Karlin, *Phys. Rev. E* **94**, 053311 (2016).
- [75] O. Filippova and D. Hänel, *J. Comput. Phys.* **147**, 219 (1998).

- [76] S. Succi, O. Filippova, H. Chen, and S. Orszag, *J. Stat. Phys.* **107**, 261 (2002).
- [77] U. R. Alim, A. Entezari, and T. Möller, *IEEE Trans. Vis. Comput. Graph* **15**, 630 (2009).
- [78] R. Gatignol, *Phys. Fluids* **20**, 2022 (1977).
- [79] S. Ansumali and I. V. Karlin, *Phys. Rev. E* **66**, 026311 (2002).
- [80] M. Sbragaglia and K. Sugiyama, *Phys. Rev. E* **82**, 046709 (2010).
- [81] J. Meng and Y. Zhang, *J. Comput. Phys.* **258**, 601 (2014).
- [82] S. Krithivasan, S. Wahal, and S. Ansumali, *Phys. Rev. E* **89**, 033313 (2014).
- [83] N. Frapolli, S. S. Chikatamarla, and I. V. Karlin, *Phys. Rev. E* **93**, 063302 (2016).
- [84] L. G. Leal, *Advanced Transport Phenomena: Fluid Mechanics and Convective Transport Processes*, Vol. 7 (Cambridge University Press, Cambridge, 2007).
- [85] R. B. Bird, W. E. Stewart, E. N. Lightfoot, and D. J. Klingenberg, *Introductory Transport Phenomena*, Vol. 1 (Wiley, New York, 2015).
- [86] C. B. Laney, *Computational Gasdynamics* (Cambridge University Press, Cambridge, 1998).
- [87] B. Larkin, in *Thermophysics of Spacecraft and Planetary Bodies* (Elsevier, Amsterdam, 1967), pp. 819–832.
- [88] M. Parang and A. Salah-Eddine, *AIAA J.* **22**, 1020 (1984).
- [89] Y. Huang and H. H. Bau, *Int. J. Heat Mass Transfer* **40**, 407 (1997).
- [90] L. W. Spradley and S. W. Churchill, *J. Fluid Mech.* **70**, 705 (1975).
- [91] A. Mazloomi M., S. S. Chikatamarla, and I. V. Karlin, *Phys. Rev. E* **92**, 023308 (2015).
- [92] J. Schumacher, *Phys. Rev. E* **79**, 056301 (2009).
- [93] R. M. Clever and F. H. Busse, *J. Fluid Mech.* **65**, 625 (1974).
- [94] S. Ansumali, S. Arcidiacono, S. Chikatamarla, N. Prasianakis, A. Gorban, and I. Karlin, *Eur. Phys. J. B* **56**, 135 (2007).
- [95] C. Thantapanally, S. Singh, D. V. Patil, S. Succi, and S. Ansumali, *Int. J. Mod. Phys. C* **24**, 1340004 (2013).